Reviews
Nanostructured, nanoscale materials and nanodevices

УДК 620.3 DOI: 10.17277/jamt.2024.03.pp.207-235

Structure control of metal-carbon composites with different nanotopological configurations and electrical conductivity characteristics in a laser experiment

© Dmitry N. Bukharov[a]✉, Darya D. Tumarkina[a], Alexey O. Kucherik[a], Alexey G. Tkachev[b], Sergei M. Arakelian, Irina V. Burakova[b], Alexander E. Burakov[b]

[a] *Vladimir State University,*
87, Gorky St., Vladimir, 600000, Russian Federation,
[b] *Tambov State Technical University, Bld. 2, 106/5, Sovetskaya St., Tambov, 392000, Russian Federation*

✉ buharovdn@gmail.com

Abstract: The paper examines the control of functional characteristics, particularly electronic transport properties, in inhomogeneous surface nanostructures of a topological class on a solid substrate, with a focus on enhancing electrical conductivity and controlling its modes in cluster-type metal-carbon composites. From the perspective of general solid-state physics, particularly for granular metals, the discussion centers on structural microcrystalline defects, specifically at the nanoscale in this case. The study involves the modeling of the formation of such systems with nanocluster structures within the context of digital materials science, demonstrating several experimental results. This is done under conditions of introducing nanotubes into a non-conductive matrix as additives with an optimal concentration, or conversely, introducing metal atoms (typically noble metals) into a nanotube system. A two-stage process is considered, involving laser ablation of various targets, including the initial stage of obtaining nanoparticles and nanoclusters with a sufficiently large number of atoms in colloidal systems in specific liquids. In the second stage, subsequent deposition onto a solid, usually dielectric, surface is implemented to create a matrix with the desired geometry and specified nanocluster topology. The studied effects and the possibility of controlling them using laser methods hold great promise for the development of micro- and nanoelectronics components and systems based on new physical principles. Trends and tendencies in the synthesis of high-temperature superconducting states in topological structures of various classes are also discussed.

Keywords: laser ablation; nanocluster models; carbon nanofibers; fractal structures; electrical conductivity; self-healing of cracks; 1-D metal-carbon assemblies of different organizations.

For citation: Bukharov DN, Tumarkina DD, Kucherik AO, Tkachev AG, Arakelyan SM, Burakova IV, Burakov AE. Structure control of metal-carbon composites with different nanotopological configurations and electrical conductivity characteristics in a laser experiment. *Journal of Advanced Materials and Technologies*. 2024;9(3):207-235. DOI: 10.17277/jamt.2024.03.pp.207-235

Управление структурой металлоуглеродных композитов разной нанотопологической конфигурации и характеристики электропроводимости в лазерном эксперименте

© Д. Н. Бухаров[a]✉, Д. Д. Тумаркина[a], А. О. Кучерик[a], А. Г. Ткачев[b], С. М. Аракелян, И. В. Буракова[b], А. Е. Бураков[b]

[a] *Владимирский государственный университет имени Александра Григорьевича и Николая Григорьевича Столетовых, ул. Горького, 87, Владимир, 600000, Российская Федерация,*
[b] *Тамбовский государственный технический университет, ул. Советская, 106/5, пом. 2, Тамбов, 392000, Российская Федерация*

✉ buharovdn@gmail.com

Аннотация: Рассмотрены в неоднородных поверхностных наноструктурах топологического класса на твердом теле вопросы управления функциональными характеристиками, в частности, электронными транспортными свойствами для задач повышения электропроводимости и управления ее режимами в металлоуглеродных

композитах кластерного типа. В аспекте общих положений физики твердого тела, в частности, для гранулированных металлов, речь идет о структурных мелкокристаллических дефектах, в данном случае – наномасштабных. В условиях внедрения нанотрубок в непроводящую матрицу как присадки с оптимальной концентрацией, или наоборот – атомов металлов (обычно – благородных) в систему из нанотрубок проведено моделирование формирования подобных систем с нанокластерными структурами в аспекте цифрового материаловедения с демонстрацией ряда экспериментальных результатов. Рассмотрена двухэтапная схема с лазерной абляцией различных мишеней, в том числе, и через первый этап получения наночастиц и нанокластеров с достаточно большим числом атомов в коллоидных системах в определенных жидкостях. На втором этапе реализуется последующее их осаждение на твердотельную, как правило, – диэлектрическую, поверхность – с получением матрицы требуемой геометрии с заданной топологией нанокластеров. Исследуемые эффекты и возможность управления ими лазерными методами имеют большую перспективу при разработке элементов и систем микро- наноэлектроники на новых физических принципах. Обсуждаются тренды и тенденции в синтезе высокотемпературных состояний в сверхпроводимости в топологических структурах разного класса.

Ключевые слова: лазерная абляция; модели нанокластеров; углеродные нановолокна; фрактальные структуры; электропроводимость; самозарастание трещин; 1-D металлоуглеродные ансамбли разной организации.

Для цитирования: Bukharov DN, Tumarkina DD, Kucherik AO, Tkachev AG, Arakelyan SM, Burakova IV, Burakov AE. Structure control of metal-carbon composites with different nanotopological configurations and electrical conductivity characteristics in a laser experiment. *Journal of Advanced Materials and Technologies*. 2024;9(3):207-235. DOI: 10.17277/jamt.2024.03.pp.207-235

Introduction

The issue of the sharp increase in electrical conductivity of various materials, including understanding the physical principles to achieve high-temperature superconducting states, has long been a key topic in many fundamental interdisciplinary studies [1].

Typically, this involves finding the appropriate elemental chemical composition and physicochemical properties of synthesized objects and solid solutions (see, for example, [2]). However, the structural configuration of these materials is also of crucial importance, especially for metal-carbon composites with various nanocluster forms, sizes, and additives, particularly carbon nanotubes (cf. [3]). The focus here is on thin-layered/multilayered surface structures of solid samples with objects of different dimensionalities – from 0D to 3D – and their combinations, which in our case are obtained experimentally through laser ablation of target surfaces with selected compositions [4].

When discussing the electronic spectra of nanocluster structures on the scale of nanometers for metals and semiconductors within the realized matrix, they can be considered similarly to conventional solid bodies. Despite this, the properties of nanocluster structures significantly differ from those of bulk samples due to the large surface area in nanocluster arrays and potential charge separation at the interphase boundary, which leads to shifts in atomic levels [3, 5]. Size effects and contact potential differences at the interfaces, such as those between gold atoms on a graphite substrate of highly oriented pyrolytic graphite due to differing Fermi levels, can result in an excess number of electrons in gold clusters (cf. [6]). The interactions that arise between these elements are also important.

In this regard, the following features of electrophysics in such compounds, which contain metallic (usually noble metals) and semiconductor nanoparticles, can be noted. Their spatial configuration and distribution are determined by controlled conditions during the selected laser experiment, which promote the emergence of correlated charge topological states in the system with defects/vacancies, leading to a sharp increase in electrical conductivity – by many orders of magnitude in some cases [7, 8]. This is determined both by the individual characteristics of isolated nanoclusters and by their interactions with neighboring clusters and with substrates of various types. We use the term «electrical conductivity» rather than the more commonly accepted «electrical conductance» to emphasize that we are referring to a discrete nanocluster structure.

Let us list a number of conditions for the manifestation of these phenomena.

Firstly, this concerns the possibility of realizing states in topological nanostructures with characteristics analogous to those found in topological insulators. These states are associated with specific boundary conditions, surface areas between constituent elements, and the trajectories of charge carriers moving through vacant regions (cf. [9]). Crucially, the topological parameters function similarly to thermodynamic parameters in phase transitions, particularly with regard to temperature. Thus, in the presence of certain surface state configurations within the matrix of nano-objects, they influence electronic states, which may become

correlated, leading to a significant improvement in electrophysical properties (cf. [10]). For instance, in such systems, electrical conductivity is realized through electron transfer along various trajectories within this matrix. However, surface concentration and the density of electronic states compared to their number in the conduction band, as well as the presence and type of various impurities and vacancies, are also important factors [11].

In our experiments, we observed a reduction in electrical resistance by up to 10^4 times in planar thin-film nanocluster structures with a specific topology [12, 13]. This suggests potential approaches and trends in the study of high-temperature superconductivity. A characteristic of this effect is a significant decrease in the density of states near the Fermi level, known as the pseudogap state, which is typical, for example, of disordered semiconductors [14]. This could also involve nanoscale disorder within the nanocluster structure. Here, we do not address effects involving quasiparticles and exciton-polariton states. Essentially, this pertains to quantum size effects.

Secondly, there is a specific nature of physical states in highly heterogeneous nanostructures with fractal dimensionality, where significant increases in local fields can be realized (for nanometer-scale objects, up to 10^8 V·cm^{-1} during laser ablation of a metal target using standard nanosecond laser radiation with pulse energy of around 0.1*J*) [15]. In such cases, the macroscopic functional properties, including electromagnetic characteristics, of these composite samples change dramatically. In metals/steels, this is typically discussed in terms of dendritic structures with varying organization [16]. Under these conditions, electron hopping processes between neighboring dendrite peaks, which are temperature-dependent, can occur. This thermally activated hopping conductivity involves variable hopping lengths (cf. [17]).

Thirdly, considering the generally increasing electrical polarizability in systems with carbon nanotube additives (with varying diameters and lengths, porous structures, and nanofibers) and the presence of 1D directions with high aspect ratios (length-to-diameter ratio up to tens of thousands), electrical resistance in such regular configurations for a given direction of charge propagation can significantly decrease [18]. However, the effect in a nanostructured matrix depends on the specific organization of charge distribution and the uniform orientation of the 1D structures in the ensemble, forming a chain (in the simplest case – a percolation chain, essentially with a functional dependence similar to metallic conductivity) [19]. This can result in high specific electrical conductivity, comparable to that of an isolated carbon nanotube, reaching approximately 10^6 S·m^{-1} [20]. This changes the material's classification based on its electrical conductivity. Significant experimental results with practical applications can be expected in the near future.

Crucially, it is the addition of carbon nanotubes, rather than other well-conducting additives, that leads to this sharp increase in electrical conductivity. However, the possibility of controlled electrical resistance at their contact points is also important [21]. This is especially significant for the sensitivity of sensor systems using carbon nanotubes and nanofibers. If there is no direct contact between neighboring such objects, charge transfer occurs, for example, through a tunneling mechanism, which exhibits a specific temperature dependence (cf. [22]).

Fourthly, even under stochastic processes in nanostructured materials, various extreme states can occur in the dynamic characteristics of charge carriers, particularly during their movement along a separatrix, bypassing scattering centers (cf. [15, 23]). This also affects the electrical conductivity.

Another topic worth considering is the twisted and intertwined ensembles of nanotubes, such as bundles and/or sponge-like structures, as well as the shape of individual carbon nanotubes that do not conform to the ideal cylindrical form. When dealing with an inhomogeneous distribution of carbon nanotubes, it is important to account for their interactions, such as Van der Waals forces [3, 24]. All of this leads to nonlinear effects in electrical conductivity, which exhibits a non-ohmic dependence and requires quantum analysis for understanding, considering a hybrid mechanism of conductivity – both within each cluster and within the matrix on which they are situated. This also depends on the concentration of clusters and the effect of charge tunneling between them, modeled as quantum wells and barriers under conditions of thermally activated hopping processes (cf. [25]).

In this partially review-based article (largely based on our own research), we have examined all of these issues to some extent in the context of controlling conductivity characteristics.

1. Basic physical principles and methodologies

In all cases involving spatially inhomogeneous heterogeneous media at the micro- and nanoscale, it is necessary to employ various models with numerical simulations and calculations for charge carriers (see section 2 below for general principles,

and section 3 for carbon nanocomposites). This applies both to diffusion processes of their propagation and to classical percolation mechanisms (where the threshold becomes negligible with the high aspect ratio of carbon nanotubes) with conductive channels [26, 27]. These channels also emerge in contacts between heterogeneous nanocluster blocks. These simple models accurately reflect the overall trend but sometimes fail to account for significant features, particularly the imperfections and inhomogeneity of carbon nanotube chains that are in contact with each other. Therefore, numerical modeling is required, incorporating additional physical concepts and using high-level programming languages (cf. [28]).

For quantum electronic states, the well-known core-shell model is constructive, allowing for single-electron states in various types of topologies within the created nanostructures [29]. In this case, it becomes possible to control the bandgap width, the depth of impurity levels, the density of electronic states near the Fermi levels, and the emergence of various resonances (e.g., plasmonic resonances in metallic objects) as a result of changes in topological features. These conductivity processes can also be threshold-based, demonstrating step-like trigger behavior (cf. [4, 7, 30]). Moreover, their charge state can be controlled in a specific manner, which is important for various practical applications. Sensor systems with nanofibers in a distributed double-cylinder structure model, analogous to the localized core-shell model, are particularly promising here [31].

The topic of this study is of particular interest in the production of artificial diamond crystals, especially within metal-carbon nanocomposite systems, which we examine in this article under laser irradiation. These crystals can crystallize into various crystallographic forms with possible different types of inclusions. The additives with carbon nanotubes, as well as the processes of surface graphitization of the diamond itself, are of fundamental importance in controlling properties such as the electrical conductivity of these structures.

Universal phenomena of twinning can occur in these materials, either with or without changes in the shape of crystal fragments. Two mechanisms of twinning are distinguished – diffusionless and diffusion-based mechanisms, analogous to the nonlinear process of mechanical twinning during martensitic phase transformations. This topic has been studied for nearly 130 years, with particular emphasis in the latter half of this period. A modern review of the research status in this field is presented, for example, in [32], but several unresolved issues remain even when considering multifactorial models. These issues pertain to the following phenomena.

The diffusionless mechanism involves the formation of oriented regions and/or layers with the alignment of the crystal lattices of the new and old phases along their boundary of contact, with a specific arrangement of atoms. For diamond, such twinning along the (111) plane, for example, generally does not create defects in the lattice structure.

The other mechanism – the diffusion-based one – is associated with the nucleation of crystallization centers followed by the attachment of individual atoms or small groups of atoms, whose diffusion determines the growth rate of the new phase crystals within the original structure and/or in the growing crystal. In this process, the modification of the crystal structure occurs due to the relative movement of atoms over interatomic distances. This phenomenon is typically considered to be associated with changes in the concentration of the original components; however, this does not apply to the transformation of graphite into diamond or the graphitization of diamond.

To briefly characterize the difference between these two twinning mechanisms, in martensitic transformations, the lattice modification involves the displacement of atoms relative to each other over distances no greater than interatomic distances, without an exchange of positions.

These patterns are generally characteristic of diamond-like compounds within this crystallographic class, which also includes compounds with varying elemental compositions.

The discussion of this twinning phenomenon is important for us because it depends on external influences and thermodynamic conditions, and we are specifically examining laser methods of such influence. In our case, we are dealing with controlled mechanisms under different modes of laser irradiation of samples, with adjustable and selectable spatial-temporal characteristics of the laser radiation – such as laser pulse duration, laser beam parameters, and the duration or scanning time of its impact on the object. This specificity of the laser experiment is crucial for the development of physical processes.

These conditions can be considered a type of laser ablation from the target surface under certain experimental conditions, leading to the formation of dislocations and stresses in areas with twinned layers, which significantly determine the functional characteristics of the samples obtained after this treatment. In some cases, this may result in the formation of quantum dots, graphene/ribbon structures, and diamond-like crystalline micro-objects

with variable lattice states (cf. [12]). Such objects are analogous to photonic crystals widely used in topological photonics, as well as lattice states with vacancies in which atoms of various elements can be embedded (cf. [3, 12, 33]), enabling different twinning mechanisms. This process can be described in terms of topological twinning.

Additionally, the properties of nanocatalysts containing metallic nanoparticles, particularly those used in the synthesis of nanotubes with record yields on an industrial scale, strongly depend on the size and shape of the nanoparticles and their associated charge effects, which influence the catalytic activity of the structures used [34].

In this context, laser ablation methods involving the agglomeration and/or fragmentation of metallic nano-objects appear to be highly promising and versatile, particularly due to the correlated relationship between the electrical and catalytic properties of the synthesized nanostructures and the specified optimal parameters.

Here, we focus on two-stage schemes involving laser ablation of various targets, including an initial stage where nanoparticles and nanoclusters with a relatively large number of atoms are produced in colloidal systems within specific liquids. In the second stage, these particles are subsequently deposited onto a solid, typically dielectric, surface, resulting in a matrix with the required geometry and topology of nanoclusters on the solid surface [4, 15, 33]. Of particular interest is the deposition of nanoparticles from the colloid onto conductive material substrates, such as highly oriented pyrolytic graphite plates (cf. [3, 35]). The difference in the experiment between these two types of substrates – conductive and non-conductive – lies in the characteristics of the charged states of nanostructures on the substrates [36]. For non-conductive substrates with metallic nanoparticles, they become charged only in ensembles with a certain quantity of them. For conductive substrates, the charged nanoparticles remain isolated (cf. [3]).

In general, the charge and field states of nanoparticles depend on their mutual arrangement. We will present various configurations of similar structures obtained in our laser experiments as a result of several technological stages; one outcome, in particular, is the sintering of a prepared nanotube ensemble on a plate doped with gold atoms (see section 4). Such systems may be of interest in the development of sensor films based on the electrical conductivity of nanocomposites, which utilize charge transfer between the contacting elements of the composite with different work functions. Of special importance here is the laser-induced graphitization of diamond, which is a dielectric but begins to exhibit semiconductor properties with tunable characteristics in certain induced structures [3, 37].

The technology of laser fragmentation used in sample production allows, on one hand, the formation of ultrathin atomic-scale layers. On the other hand, it enables the synthesis of isolated quantum dots, which can be the basis for creating laser diode sources in desired spectral ranges. This refers to quantum-sized nanostructures of different classes. Of particular interest are quantum cascade lasers, which involve transitions between electronic states within a quantum well of a single band, rather than the usual electron-hole recombination system (with transitions between the conduction and valence bands) (cf. [15, 38]).

However, in this work, we will focus solely on the structural and topological aspects of controlling electronic transport properties to enhance electrical conductivity and manage its modes in such structures. In the context of general principles of solid-state physics, particularly for granular metals, we can discuss structural fine-crystalline defects, which in this case are nanoscale. We will also consider (see section 3.5) a certain structural helical model for electrical conductivity in a specific stable configuration. An analogous configuration may be achievable in a laser experiment with a specific strategy: scanning the laser beam with a selected laser pulse duration.

When it comes to embedding nanotubes into a non-conductive matrix as additives with optimal concentration, or conversely, embedding metal atoms (usually noble metals) into a nanotube system, the interactions between them become important. In section 4, we will examine the second case of such a composite – sintering a nanotube powder with gold atoms using graphite-shungite.

2. Modeling of nanocluster complexes using noble metals in colloidal systems under laser exposure

We present a universal model for synthesized nanoclusters on a solid substrate surface. This model can be applied to clusters of any composition, but for clarity and further discussion, we will consider a system of noble metals (cf. [15]).

Colloidal systems of noble metal nanoparticles (Ag, Au) were formed by exposing bulk targets (composition: Au – 99.9 %, Ag – 99.9 %) placed in liquid media to laser radiation of moderate intensity (up to 10^6 W·cm^{-2}) at a wavelength of 1.06 μm. To deposit nanoclusters from the solution onto a substrate, we used a method of thermodiffusion

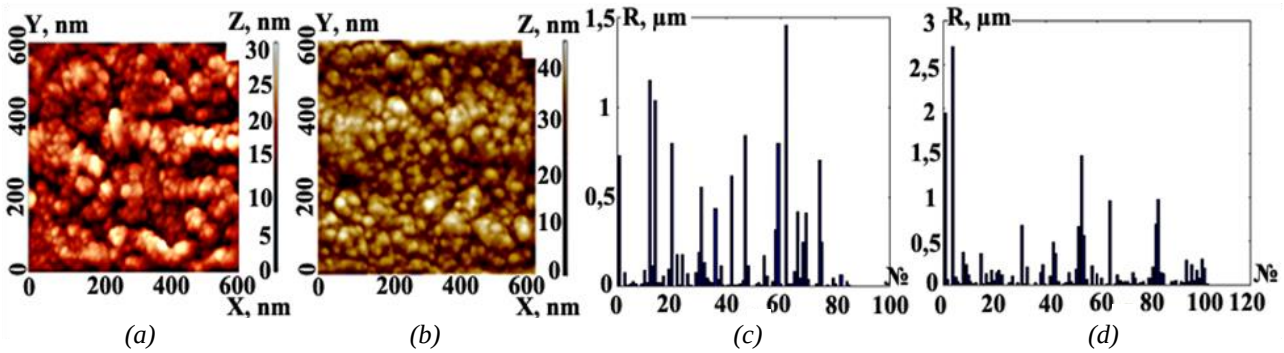

(a) *(b)* *(c)* *(d)*

Fig. 1. AFM images of bimetallic (Ag/Au) nanocluster systems at a laser beam scanning speed of 1.2 mm·s^{-1} after 15 (*a*) and 20 (*b*) passes. The size distribution (spatial scales are shown on the axes) of the objects in the samples: for Fig. 1*a* – with the histogram (*c*) and for Fig. 1*b* – with the histogram (*d*); the vertical axis indicates the object sizes *R*, and the horizontal axis indicates the numbers of the studied objects

deposition onto glass from a colloidal solution obtained by intensively mixing noble metal nanoparticles (Ag, Au, and/or Ag/Au mixture, with an average particle size of 100 nm) with glycerin [39]. After laser exposure, the colloidal systems were studied using a Horiba LB-550 particle size analyzer based on dynamic light scattering. Images of the nanostructures deposited on the substrate were captured using a Quanta 200 3D scanning electron microscope and an Integra-Aura probe nanolaboratory.

The study of the sample surface (Fig. 1), conducted using the MATLAB Image Processing Toolbox [40], revealed the clustered nature of the nanoparticle system, with well-defined agglomerates ranging in size from 1 to 3 μm and average heights from 10 to 40 nm, as seen in the images obtained using atomic force microscopy (AFM) (Fig. 1*a*, *b*).

When deposited from single-component colloids (Ag or Au), the synthesized systems consisted of isolated fractal nanocluster dendrites with a disconnected surface topology (Fig. 2). Objects ranging from 10 to 300 nm were clearly visible. Their sizes exceeded those of the nanoparticles in the original colloidal system (5–20 nm). This observation indicates the thermodiffusion nature of the formation of nanocluster systems, with a preliminary aggregation process of the nano-objects in the colloidal solution prior to deposition on the substrate.

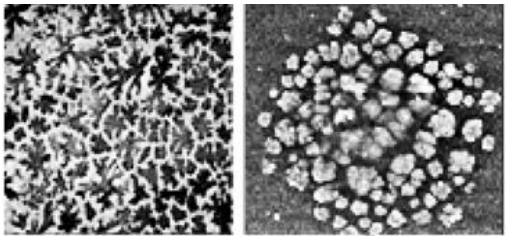

(a) *(b)*

Fig. 2. AFM images of the Ag (*a*) and Au (*b*) nanocluster systems

When forming nanocluster systems from a two-component colloidal solution (Au/Ag at a concentration ratio of 50/50), samples with a more heterogeneous and sparse spatial structure of a cluster nature were obtained. However, the process resulted in the unification of objects into a single structure, similar to alloy formation, in this case with a connected surface topology. This observation suggests the presence of melting in the system with nano-objects during the formation of this unified cluster.

However, we did not consider the thermodynamic processes for this mechanism, which would require calculations of the entropy values for such alloys (this is a separate task, which we have conducted for diamond-like compounds, specifically in [12, 33]). Here, we were only interested in classifying them by their fractal dimension values. The fractal dimensions of the obtained samples were estimated using the box-counting method [41], which confirmed their dendritic nature. For example, the fractal dimension of the sample in Fig. 2*a* was $D = 1.898$, and for the sample in Fig. 2*b*, it was $D = 1.922$. These values are quite consistent with the estimates of fractal dimensions of dendritic structures known from the literature [42]. The accuracy of determining these numerical values of D corresponds to the standards accepted in fractal mathematics (cf. [23]).

The modeling of the cluster formation process was carried out within the framework of diffusion-limited aggregation (DLA) [43], which describes aggregates both in the colloidal system and in their structures deposited on a solid surface.

In general, the algorithm for forming DLA structures is implemented as Brownian motion of a particle within a computational domain containing a seed structure, followed by aggregation/attachment with a given probability. Various modifications of the

general DLA case allow for the consideration of thermal processes occurring during aggregation in colloidal systems. The DLA model and its transformation, taking into account additional factors, can be implemented using cellular automata techniques with von Neumann and/or Moore neighborhoods [44]. For instance, using the von Neumann neighborhood allows for the creation of samples with a heterogeneous structure, while the Moore neighborhood produces well-filled, homogeneous samples (see more details in the Appendix).

To describe convective flow in the region heated by laser radiation, it is convenient to use the standard Rayleigh-Bénard model (in the case of a point heater located at the bottom) for planar geometry within the Boussinesq approximation [45], accounting for its rotation by a certain angle. We employed this model to estimate the resulting nanocluster configurations in a controlled manner (cf. [15]) with the corresponding temperature field [46] on the substrate.

By varying the probability of agglomeration (adhesion) *s*, it is possible to model dendritic structures of various shapes (Fig. 3). For small values of the adhesion probability, well-filled, fairly homogeneous clusters with a smooth boundary and a fractal dimension *D* of about 1.85–2.02 are formed. For large values of the adhesion probability *s*, heterogeneous clusters with a highly jagged boundary and a lower fractal dimension $D \sim 1.70$–1.85 are formed. For instance, the model in Fig. 3 can be correlated with certain elements of the nanocluster system in the samples from Fig. 2*a*, *b*. In this case, there is a qualitative similarity between the topologies of the model and the experimental sample.

The conducted studies revealed the fractal nature (following a diffusion mechanism) of the structures, which corresponded to the selected approximation during modeling. The initial distribution of seed structures within the computational area, as well as the adhesion probability s, influences the shape of the aggregates. For instance, Fig. 4 shows 3D model images of DLA clusters in a.u. based on a cellular automaton in the von Neumann neighborhood. The cluster systems were formed within a sphere at the center of the computational area for the case $s < 1$ (Fig. 4*a*) and $s < 0.1$ (Fig. 4*b*), as well as in the case of aggregation from a point at the center (Fig. 4*c* and 4*d*).

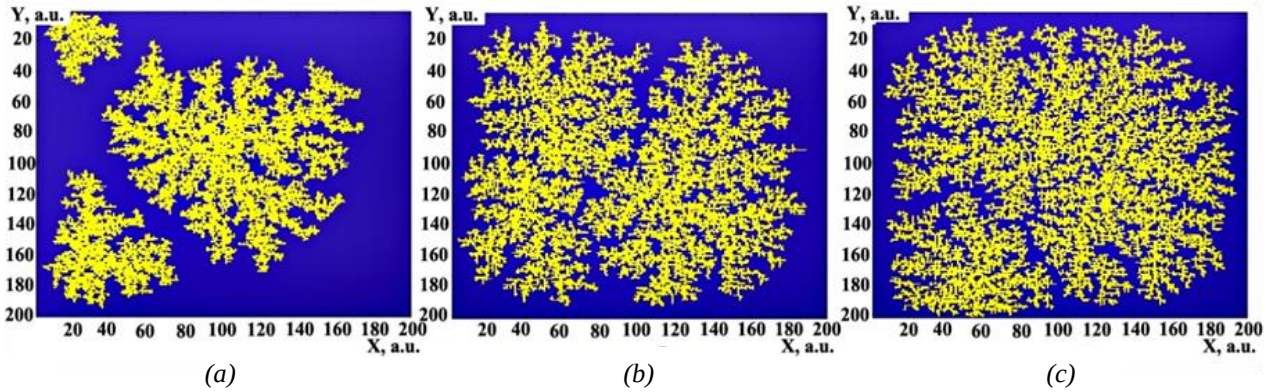

(a) *(b)* *(c)*

Fig. 3. A variety of fractal structures on a relative scale, generated by varying the adhesion probability *s*. As an example, starting with three aggregation centers (clearly visible in Fig. 3*a*): with a parameter value of $s = 0.1$, we have $D = 1.85$ (*a*); with $s = 0.5$, $D = 1.80$ (*b*); and with $s = 1$, $D = 1.79$ (*c*)

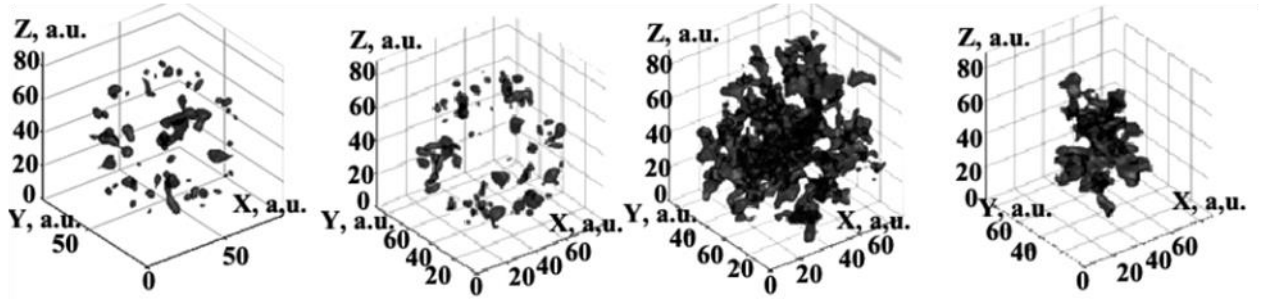

(a) *(b)* *(c)* *(d)*

Fig. 4. DLA clusters: A seed within a sphere at the center, where an aggregate is formed with probability $s < 1$ (*a*); $s < 0.1$ (*b*). The seed is at the center, and the aggregate forms across the entire computational domain for two values $s < 1$ (*c*); $s < 0.1$ (*d*)

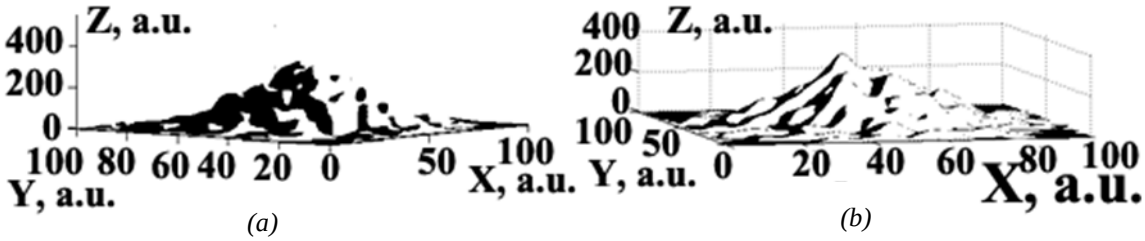

(a) *(b)*

Fig. 5. DLA structure of clusters with varying height *h*, deposited on a surface: when *s* = 1 (*a*); when *s* depends on the current maximum height of the emerging structure (*z* – axis) with a maximum selected dendrite height of *H* = 240 a. u. (*b*)

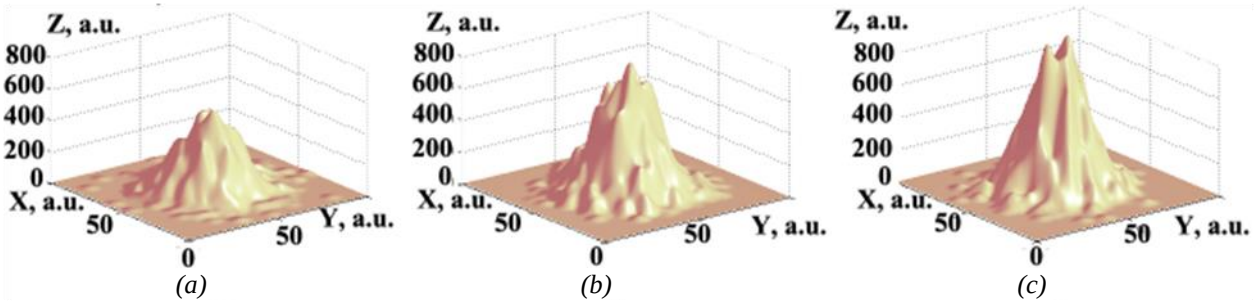

(a) *(b)* *(c)*

Fig. 6. Model of the deposited structure with *s* =1 (*a*); *s* = 0.5 (*b*); and with a continuous decrease over time of *s* values from the initial value of 1 to the final value of 0.001 (*c*)

Figure 5 shows model qualitative images of a system of fractal/dendritic nanoclusters in Cartesian coordinates in a.u., deposited from a colloidal solution onto a solid substrate. They were formed within the framework of the DLA model, where a horizontal plane (*x*, *y*) was chosen as the seed structure, and the value of *s* was set to 1 (Fig. 5*a*). The case was also considered where the variable value of *s* depended on the current maximum height *h* of the forming structure, as shown in the figure (Fig. 5*b*). This value increases to the required maximum height *h* = *H* (see Fig. 6). In this model, we assume that *s* = *h*/*H*, so that over time, the value of *s* increases from 0 (*h* = 0) to 1 (*h* = *H*).

Figure 6 shows the qualitative dynamics of changes in the cluster structure when determining the value of the parameter *s*.

From Figure 6, it can be concluded that a high adhesion probability *s* allows the formation of structures that are not tall but have a wide base. Conversely, small values of *s* lead to cluster systems consisting of long, narrow "nanopeaks".

The comparison of simulation results (Figs. 4–6) with the experiment (see Figs. 1 and 2) showed a qualitative agreement, indicating a good level of adequacy of the proposed model.

The computational experiments and their statistical analysis demonstrated that the DLA model allows the creation of fractal clusters with dimensions ranging from 1.67 to (2.02 ± 0.03) when varying the adhesion probability s within the interval [1; 0.01] (Fig. 7). Values exceeding a dimension of 2 suggest the formation of 3D structures.

In turn, the temperature dependence of the fractal dimension *D* can be represented as (compare with [25, 45]):

$$D(T) \sim A_0 T^{\alpha},$$

where A_0 and α are some empirical proportionality coefficients.

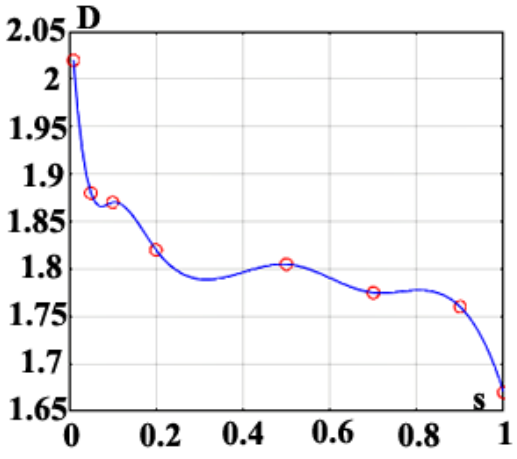

Fig. 7. The dependence of fractal dimension *D* on the adhesion probability *s*: points represent the calculated values, and the line represents the approximation, taking into account cubic spline interpolation in MATLAB [40]

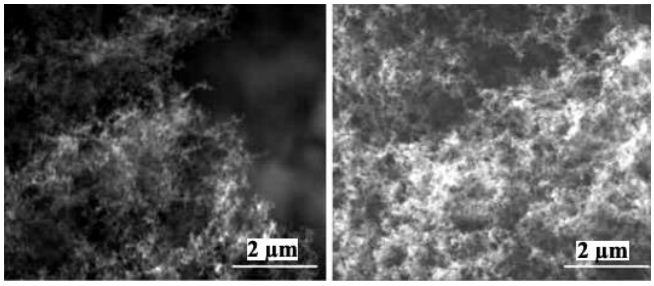

(a) *(b)*

Fig. 8. SEM images of nanofibrous carbon structures subjected to the same laser beam but with different values of external electric voltage applied to the sample: 1 kV (*a*), 0.8 kV (*b*) [48]

The anisotropy of the computational domain can be defined through the temperature field in the laser beam (see [4]). Then, with the temperature distribution in the plane case on the substrate surface in the form of a system of isothermal regions, it becomes possible to estimate the adhesion probability for a wandering particle upon entering a given isothermal region (compare with [39]). In this case, the random displacements of the particle during its wandering are not equally probable. This method of accounting for anisotropy allows consideration of the direction of particle diffusion into the laser heating area as an increased probability of random displacements (see [46]).

3. Modeling the carbon nanofiber system

In this section, we will examine in detail models involving carbon materials based on nanofibers, which are promising, for example, in the development of nano-microelectronics components and systems [3, 15, 47].

One convenient method for synthesizing carbon nanofibers is by exposing the medium to laser radiation in the presence of an external electric field. Using this method, as described in [48], we obtained carbon nanofibers deposited on a metal plate (Fig. 8). The structure of the synthesized samples indicates the controllability of the topological characteristics of nano-objects by selecting appropriate experimental parameters: laser radiation characteristics and the intensity of the externally applied electric field. For instance, Figure 8 shows a sample nanofiber structure at various specified external voltages.

3.1. General principles

The obtained samples, under different values of control parameters, were studied using scanning probe microscopy (SPM) and Raman spectroscopy. The morphological properties were investigated through fractal analysis of the dimensions of the nanofiber images obtained with a scanning electron microscope; this analysis was conducted using the box-counting method [49]. Depending on the deposition time and the power of the laser radiation source, it is possible to control the fractal dimension value. For example, it gradually increased from 1.45 to 1.9 with laser radiation power of 30 W; from 1.6 to 1.96 with a power of 50 W; and from 1.75 to 1.98 with a power of 100 W, while the deposition time under laser radiation remained constant in all cases.

As mentioned above, a convenient model that allows for generating structures with fractal dimensions and accounting for thermal processes is the DLA model [49, 50]. The nanofiber model in the DLA approximation was implemented as a cellular automaton with a Moore neighborhood [51] (see Appendix P.1). The influence of the medium's thermodynamic characteristics was accounted for in the aggregation/adhesion probability coefficient *s*, which was represented as a normalized diffusion coefficient within the interval (0; 1].

Figure 9 shows model images of nanowires (filamentary objects) with nanofragments (though in a. u., they depend on the control parameter – adhesion probability *s* and branches on their predominantly linear structure in the DLA approximation within a computational domain of 300×300 a. u. for 30,000 particles. In Figure 9*a*, the case of equal-probability displacement of diffusing nanoparticles with a constant $s = 1$ is shown. Figure 9*b* presents a model of the nanowire system with small lateral displacements of the diffusing particles and a uniform decrease in the adhesion probability from 1 to 0.01. Figure 9*c* depicts a nanowire system with small lateral displacements of diffusing particles and a uniform decrease in the adhesion probability s, from 0.5 to 0.01. The case of small lateral displacements of diffusing particles allows for qualitatively accounting for the effect of the applied external electric field, where the structure growth occurs predominantly along the lines of the field's intensity. The above-mentioned change in adhesion probability corresponds to the cooling of the system after laser exposure, analogous to experimental conditions. In both cases, the generation process stopped when the nanowire reached the upper boundary of the computational domain. Comparing Figures 9*a*, 9*b*, and 9*c*, it can be concluded that the probability of random lateral displacements affects the shape of the nanowire. In the case of low lateral displacement probabilities, the nanowires generated are more vertically elongated with smaller and fewer lateral branches.

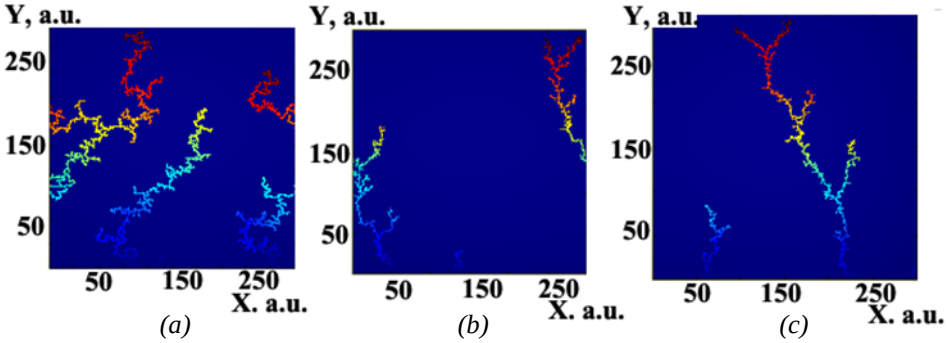

Fig. 9. Models of nanowire systems in the DLA approximation:
(*a*) equal-probability displacements of diffusing particles with a constant value of $s = 1$;
(*b*) small lateral displacements of diffusing particles with a uniform decrease in s from 1 to 0.01;
(*c*) uniform decrease in s from 0.5 to 0.01

Switching to absolute units allowed for a comparison between the model and experimental results in terms of assessing the local lengths of the simulated fractal nanostructures. By setting the side length of the computational cell in the model to 10 nm, the maximum length of the nanowires was found to be between 3000 and 3900 nm in the case of equal-probability displacements. This may correspond to the generation of nanowires in the presence of a weak external electric field. The range of maximum lengths, from 3000 to 3400 nm, in the case of small lateral displacements is characteristic of nanowires generated under a stronger electric field.

These values qualitatively match the results of experimental measurements, and the models used can be useful for predicting and evaluating the geometric properties of nanowires (cf. [48]).

3.2. Laser-induced 1D carbon filamentary fractal structures on solid surfaces: models and experimental implementation

The electrophysics of systems with different spatial dimensionalities (from 0D to 3D) is related to symmetry factors and their modification under conditions of topological phase transitions. This determines various electronic states that depend on the shape, size, and spatial distribution of such objects, typically on the surface of a solid body (see, for example, [4, 52]). Recently, such systems have been intensively studied in terms of "strange" crystalline/metallic structures [53] and other specific objects [54], which are important for practical applications.

The key control parameters here are the dimensional ratios, such as the distance between clusters r compared to their size l, and/or similar ratios within each cluster for nanostructures within it. The physical significance lies in how deeply (h) into a given topological object – a cluster or its elements – interactions from their surroundings penetrate. For the entire cluster array on the substrate, this concerns its extent L compared to the size of one cluster l, meaning the ratio of these parameters can be very large (cf. [15, 55]).

This is associated with pairwise interactions between nearest neighbors, which define nonequilibrium/strained states on their separating surfaces (cf. [56]). Specifically, as the surface area with negative surface tension increases, such states become thermodynamically more favorable in energy terms. Although the general process of forming these objects with negative surface tension is unstable, under extreme conditions—such as laser ablation in a liquid – it can be considered locally isobaric, fixing the configuration of objects and maintaining it when returning to normal conditions (cf. [15]). This significantly alters the functional characteristics of samples with a specific array of these structures, which is quite controllable.

Such surface effects in a thin layer were observed in our experiments [12, 13, 57], where, depending on the topology of the fractal surface cluster configurations, the electrical resistance of the sample could decrease significantly – up to 10^4 times – under similar resistance measurement schemes across the homogeneous surface area of the sample (see, for example [7]).

In this context, carbon (C) compounds, including their combinations with noble metals [58, 59], are of great importance. In particular, this includes long linear carbon chains LLCC [60], which exhibit unique properties. These structures form, for instance, when LLCCs are fixed at the edges between atoms of noble metals, such as two gold (Au) and/or silver (Ag) atoms, and they are stable. This involves actual phase transitions to a new allotrope form of carbon [4, 61].

A separate issue is the creation of metasurfaces based on such LLCCs (sp-electron configuration) [62] when they are deposited on the surface of a solid substrate by methods such as spraying-jet [57, 60].

In all cases, both cumulene bonds $(=C=C=C)_n$ with a bond energy of 0.41 eV and polyyne bonds $(–C\equiv C–)_n$ with a bond energy of 1 eV can arise, stabilized by a 1D structure; in our case, with noble metal atoms at their ends. These objects are particularly important for practical applications in conditions of spatial orientation in external fields [63].

In our work [64], we experimentally observed a sharp nonlinear increase in the magnitude of the electric current – by tens of times – compared to the value according to Ohm's law in such a compound (Au–C–Au): in a thin film with a thickness of 30 nm, for an applied external voltage of 1.5 V, the current was 0.5 A. This LLCC object was synthesized in a two-stage laser experiment [12, 13, 58, 60]: first, using laser ablation of a shungite sample to obtain a colloidal system with nanostructures, and then through laser deposition (considering fragmentation effects) from the colloid onto a solid substrate. The formation of LLCC objects was monitored using luminescence spectra and Raman spectroscopy. This effectively implemented a 4D technology for synthesizing such objects, where besides the three spatial parameters of the structures, the fourth parameter – time – was crucial, related to both the experimental fixation of the exposure time of the used system and the chosen duration of the laser radiation exposure (cf. [65]).

In the latter case, for example, nonequilibrium phase transitions of a certain type occur under femtosecond light pulses, leading to the formation of structures with different dimensionalities [12, 65–68].

In our work, an experiment on the laser fragmentation of colloidal systems consisting of amorphous carbon was conducted under an applied external electric field of low intensity (voltage of 12 V with a distance of 3 mm between electrode microcontacts). In this case, strong polarization of the formed carbon molecules was observed, leading to the formation of extended wires when deposited on a substrate. Although these were not isolated wires but rather a tangle of these wires, their preferential growth (1D structure) still manifested in one direction along the field.

We modeled this process of geometric nematicity in the approximation of not a gaseous atomic carbon system, but an ensemble of forming C_2 and C_4 molecules – i.e., when we have 2 or 4 carbon atoms in the form of one linear molecular structure, as confirmed by luminescence and Raman spectra measurements. The final structures have spectra with maxima characteristic of objects with carbon chain lengths from 8 to 24 carbon atoms, as registered by transmission electron microscopy.

Figure 10 shows images of carbon structures obtained using transmission electron microscopy (TEM) (dark lines) under different scanning conditions at a laser beam speed v, depositing nanoparticles from the colloid onto the synthesized system on a dielectric quartz substrate with a fixed direction of the applied external electric field $\vec{E}_0$.

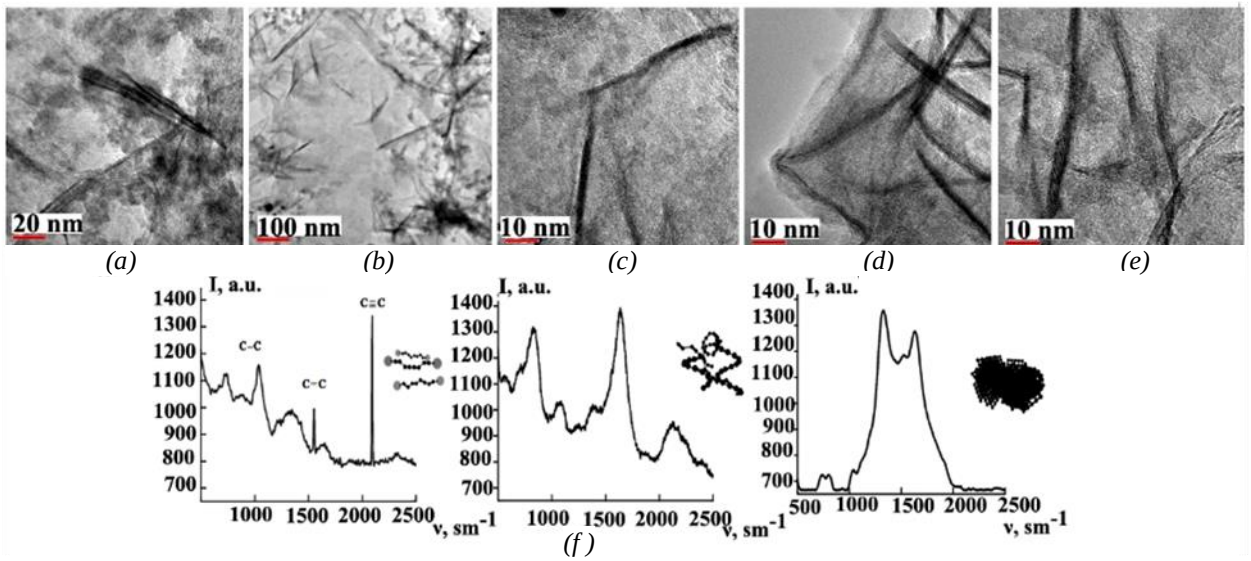

Fig. 10. TEM images of carbon LLCC structures at different scanning speeds v of the depositing laser beam and with a fixed direction of the applied external electric field $\vec{E}_0$:
v = 0.2 mm·s^{-1} (*a*), v = 0.4 mm·s^{-1} (*b*), v = 0.6 mm·s^{-1} (*c*), v = 0.8 mm·s^{-1} (*d*), v = 1 mm·s^{-1} (*e*). Modification of Raman spectra of different types of carbon structures in the colloid from which they are deposited onto the solid surface (*f*)

Although this LLCC ensemble structure generally only demonstrates 1D-directional dominance fragmentarily, it can manifest with bends and curves, as well as twists into certain configurations with bundles – so-called sponges (see below, Fig. 17). However, their spectral characteristics allow these objects to be identified as LLCCs (see [4]).

Thus, the existing inhomogeneities in the samples are not static objects but can change dynamically during the processes occurring at different scanning speeds of the laser beam across the object.

It should be noted that cracks may also appear on the substrate surface with the forming carbon structure for various reasons. Their development dynamics – exemplified by spontaneous healing – is discussed in the following section 3.3.

3.3. The process of crack self-healing

In the presence of an inhomogeneous cracked structure, the process of self-healing of existing inhomogeneities may occur under dynamic object movement conditions. This is modeled within the framework of the mechanism of particle self-diffusion.

Figure 11 presents a DLA model for the case of crack healing from three sides, with varying adhesion probability (*s*). This effect can be considered as the healing of crack ends.

Figure 12 presents a DLA model for the case of crack healing from two sides with varying adhesion probability (*s*). This effect can be viewed as healing from the center of the crack.

Figure 13 presents a DLA model for the case of crack healing from one side.

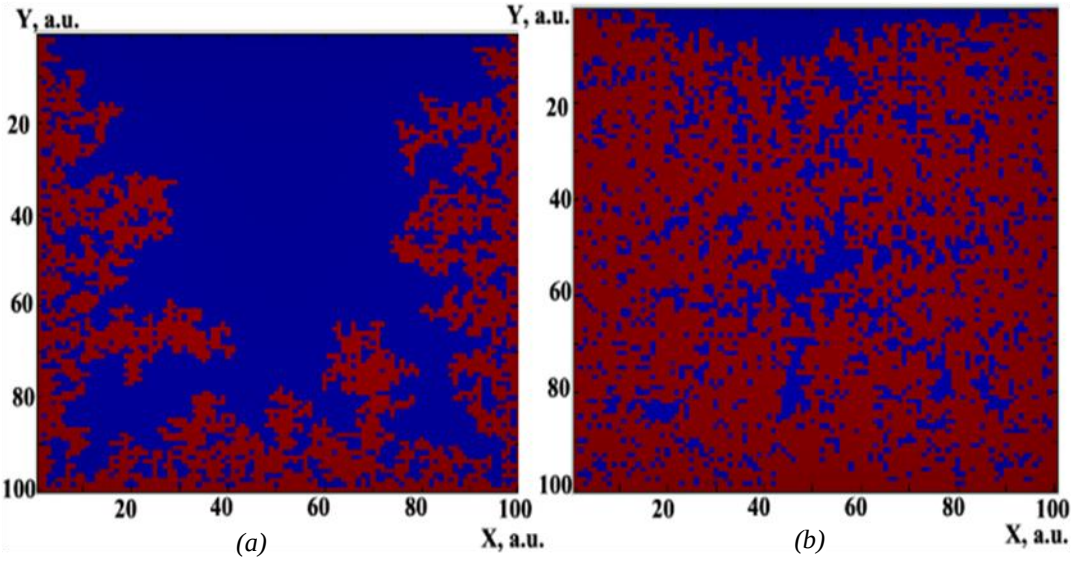

Fig. 11. Model of crack healing from three sides with varying adhesion probability (s): *s* = 0.1 (*a*); *s* = 0.3 (*b*)

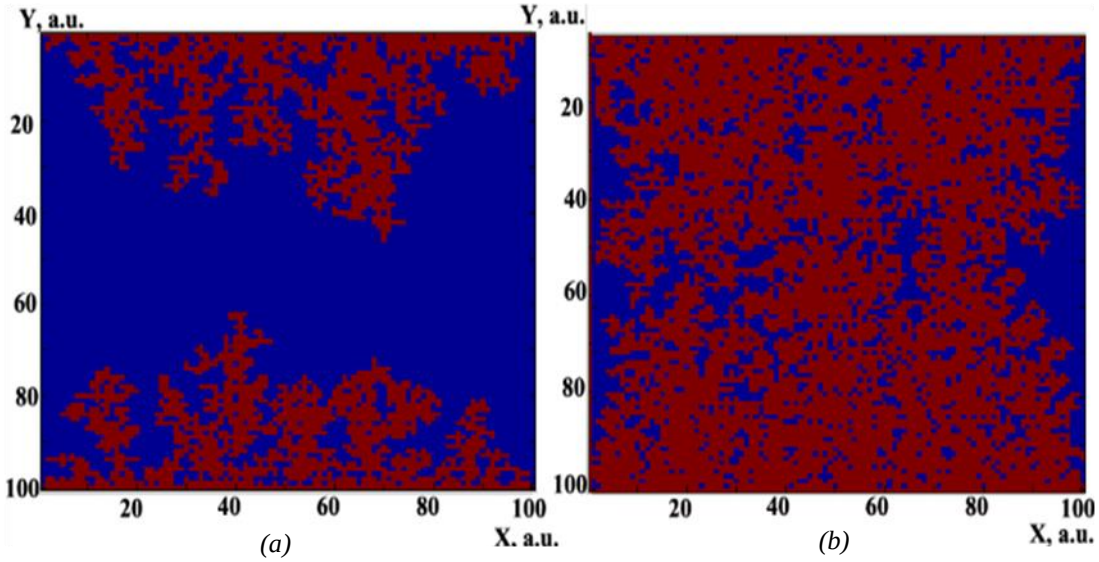

Fig. 12. Model of crack healing from two sides with varying adhesion probability (s): *s* = 0.1 (*a*); *s* = 0.3 (*b*)

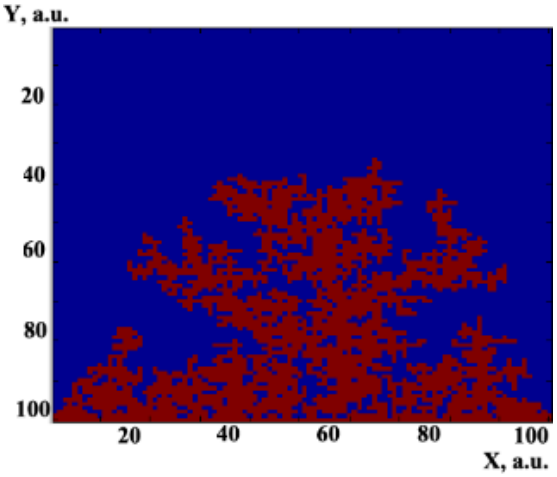

Fig. 13. Model of crack healing from one side at $s = 0.1$

Let us consider two physical models of such crack healing.

Deposition model. In the proposed models (see Appendix P.2), the computational domain is represented as a rectangular grid with dimensions $M \times L$, and particles are deposited along the vertical direction onto the previously formed structure according to specified rules, adhering to the nodes of the square grid. Over time, this process forms a cluster or aggregate with a specific geometry [69, 70].

Figure 14 shows the simulated profile from a side section of the crack, illustrating the boundaries where it contacts the surrounding material. Two crack healing structures $h(i)$ with a height of 250 a. u. over time $T = 100$ a. u. are shown, with a deposition rate of 100 (Fig. 14*a*) and 200 (Fig. 14*b*) particles per unit time (per second) within the framework of the ballistic deposition model.

A similar image is shown in Fig. 15 for another model – random deposition.

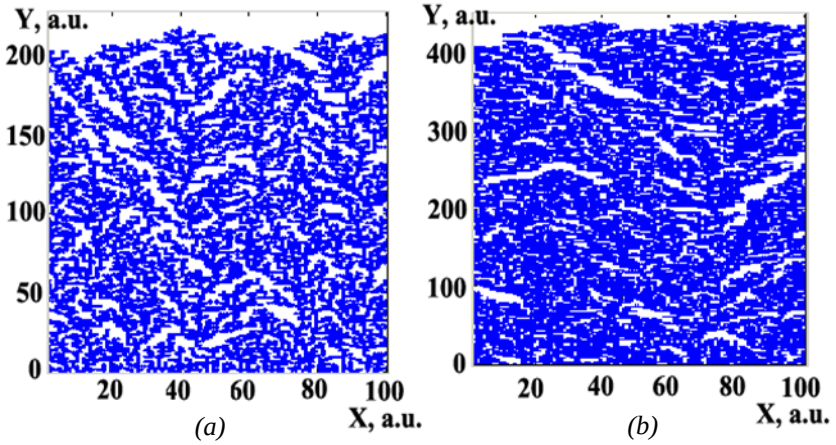

Fig. 14. Profile of the structure formed during crack healing within the ballistic deposition model at a deposition rate of 100 particles/s (*a*) and 200 particles/s (*b*)

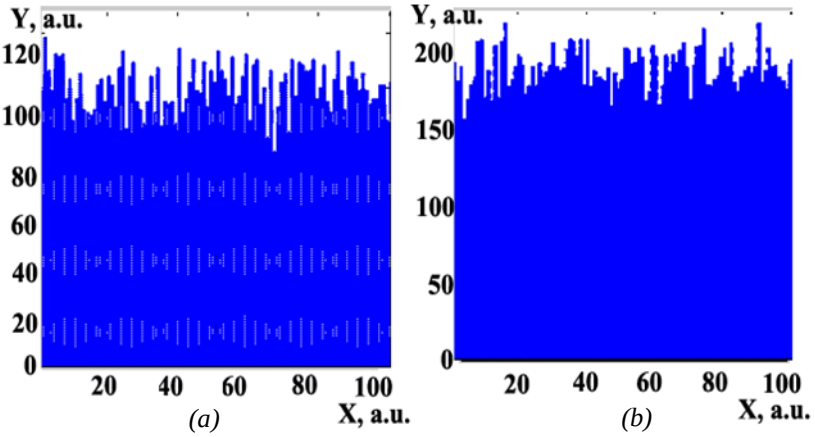

Fig. 15. Profile of the structure formed during crack healing within the random deposition model at a deposition rate of 100 particles/s (*a*) and 200 particles/s (*b*)

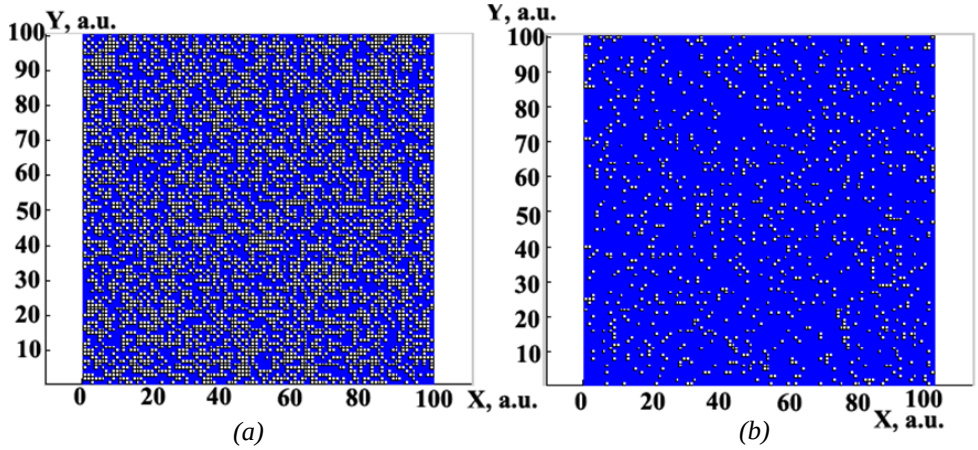

(a) *(b)*

Fig. 16. Profile of the structure formed during crack healing within the cellular percolation model at $s = 0.5$ (*a*) and $s = 0.9$ (*b*) on a plane (in a. u. along the axes)

Percolation model. In this model, the crack is represented as an aggregate of defects. The process of particles seeping into the crack from the material is considered within the percolation approximation (cf. [71]).

Figure 16 shows a simulated profile (side section) of the structure formed during crack healing within the framework of the cellular percolation model, with variations in the percolation threshold, which is determined by the value of *s*.

3.4. Diffusion model of the structure of C–Au atoms in microsponge objects

As previously discussed, one of the convenient and straightforward methods for synthesizing carbon microstructures is laser deposition from a colloidal solution containing both carbon chains and noble metal nanoparticles, which act as catalysts for the synthesis. Using this method, we obtained experimental samples that were used to develop a structural model and evaluate its adequacy. The carbon microthread system (microsponge) samples were synthesized by laser exposure, using a ytterbium laser, on a colloidal system containing carbon chains (C) and gold nanoparticles (Au) in the presence of an external electric field (Fig. 17) [72].

Analysis of the conditions and results of the experimental synthesis led to the conclusion that the process influencing the shape of the sponge had a thermodiffusion nature. The investigation of the thread system's shape revealed its branched nature, characteristic of dendritic objects formed by diffusion processes. The sponge's shape was elongated in the direction of the electric field lines in the medium. This observation served as the criterion for selecting the appropriate modeling approach.

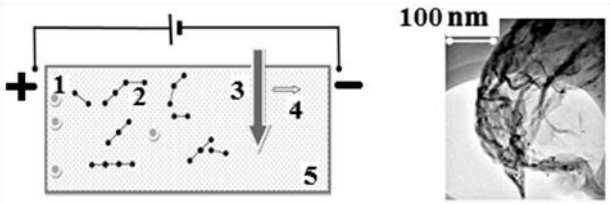

(a) *(b)*

Fig. 17. Synthesis scheme and results: experimental setup with an external electric field (*a*): *1* – Au nanoparticles; *2* – C chains; *3* – direction of laser radiation exposure; *4* – direction of laser beam movement; *5* – cuvette with colloidal solution; (*b*) – obtained optical image of the C–Au sponge

Thus, the model (see Appendix P.3) was chosen within the framework of the diffusion approximation, based on the particle diffusion equation. The model equation was solved in a discrete form using the DLA approximation [62] through an iterative process [73, 74].

The proposed model was implemented in MATLAB using a.u. Calculations of the sponge structure were performed according to this approximation, followed by a comparison with experimental samples. In the model calculations, three types of C chains were generated: objects of length 2 a. u. were introduced into the computational domain with a probability of 70 %; length 4 a.u. with a probability of 20 %; and length 5 a. u. with a probability of 10 %. Their orientation was also specified – 90 % of the chains were vertical, and 10 % were horizontal. Figure 18 shows the model of a C–Au sponge branch for a computational domain of 300 × 300 a. u. with the specified parameters, as well as the variation in sticking probability s from 0.1 to 0.2 a. u. when a single Au particle is placed at the bottom boundary of the computational domain.

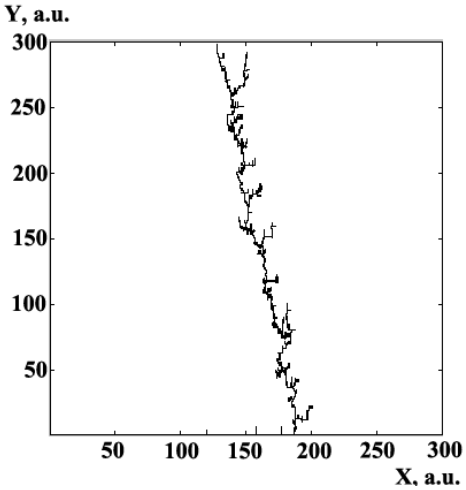

Fig. 18. Model of a C–Au sponge branch (explanations provided in the text)

The self-assembly of metal-carbon nanosponge structures was carried out by us in colloidal solutions under the influence of laser radiation and an external electric field (cf. [72]). The samples obtained in the experiments had a structure consisting of an array of nanothreads forming a sponge with micro/nano fragments, as shown in Fig. 17*b*.

Figure 19 shows a fragment of the formed random sponge structure with a system of nanothreads ranging in size from 2 to 300 μm.

Figure 20 presents a model image of a microfiber system forming a microsponge with a thread width of about 100 nm, varying the length and number of microthreads. In Figure 20*a*, the model shows short threads forming a rounded shape with a distinct small central area and long branches; 50 threads were generated for this formation. Figure 20*b* depicts a model of a sponge made of medium-length threads. The resulting figure, composed of 150 threads, is more uniform with a well-filled center and a larger area; the shape is approaching rectangular.

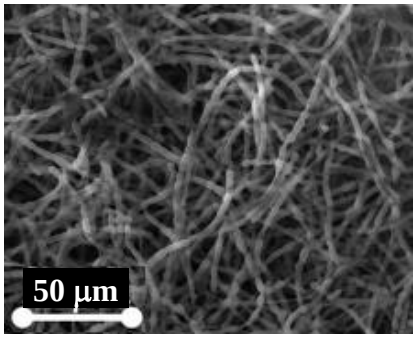

Fig. 19. Optical image of a fragment of the microsponge, part of the entire sponge shown in Fig. 17

Figure 20*c* shows an image of a sponge made of 300 threads – a rectangular shape without a distinct center and with short branches.

The simulation results qualitatively match the experimental results (Figs. 17*b*, 19).

As a model for describing individual threads in the microsponge, the Monte Carlo method [75] was considered. In this approach, objects of various sizes were introduced into the computational domain, where they made random movements and combined with a given probability. The combination of objects was considered within the framework of the Moore neighborhood (see Appendix P.4).

This approach may be useful for a first approximation in describing the experimental samples of C–Au microsponge formation.

3.5. Computer simulation of helicoidal microstructures

Helicoidal multilayer microstructures made of different materials are of interest in the context of digital materials science models due to their unique physical and functional properties (see, for example [76]).

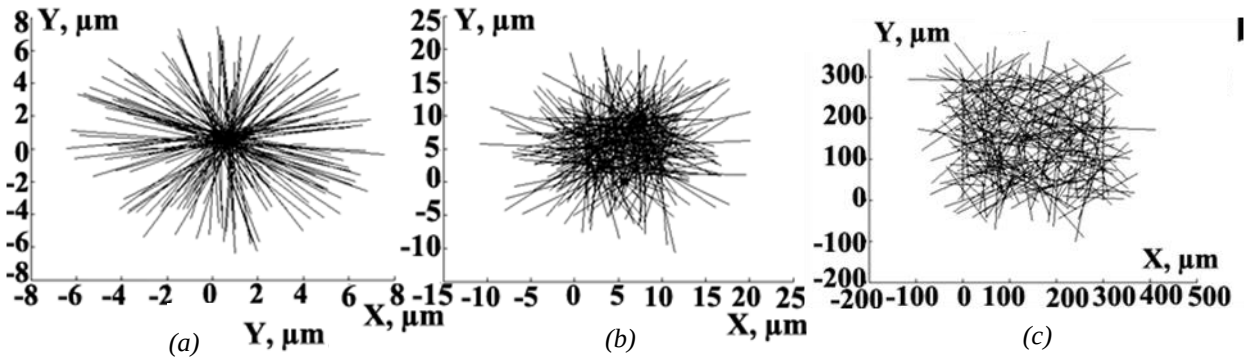

Fig. 20. Microsponge model with different thread lengths: 1–20 μm (*a*); 10–50 μm (*b*); 50–300 μm (*c*)

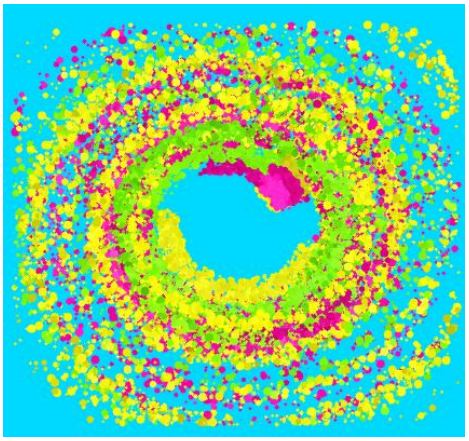

Fig. 21. Model of a helicoidal structure

The corresponding model (see Appendix P.5), which allows for the description of the structure of such objects, can be approximated as a random spiral [77]. This type of object is formed from a system of random spirals. These figures have randomly positioned centers and random radii r of the coils. They consist of points arranged along a spiral, considering random current rotation angles θ, with their coordinates defined by simple expressions: $r = r(\theta)$; $x = r\cos(\theta)$; $y = r\sin(\theta)$ [78].

Figure 21 shows an image of such a random spiral structure formed by a system of rounded objects.

A diffusion model based on a cellular automaton was implemented in MATLAB on a square computational domain with a side length of 450 a. u. The probability of a cell being occupied was assumed to be 0.5, which, in the context of this helicoidal symmetry, corresponded to the presence of an external magnetic field in the experiment. We considered a magnetic field strength of 100 Oersted (cf. [79]).

Calculations of the resulting helicoidal structures were performed using the proposed model. To account for their formation, a spiral was considered as the initial structure from which growth occurred to produce helicoidal objects. The shape of the elements forming the structure was varied in the calculation. The final figure was composed of single elements forming horizontal, vertical, and diagonal chains; for specificity, these chains were made of two and four elements (Fig. 22).

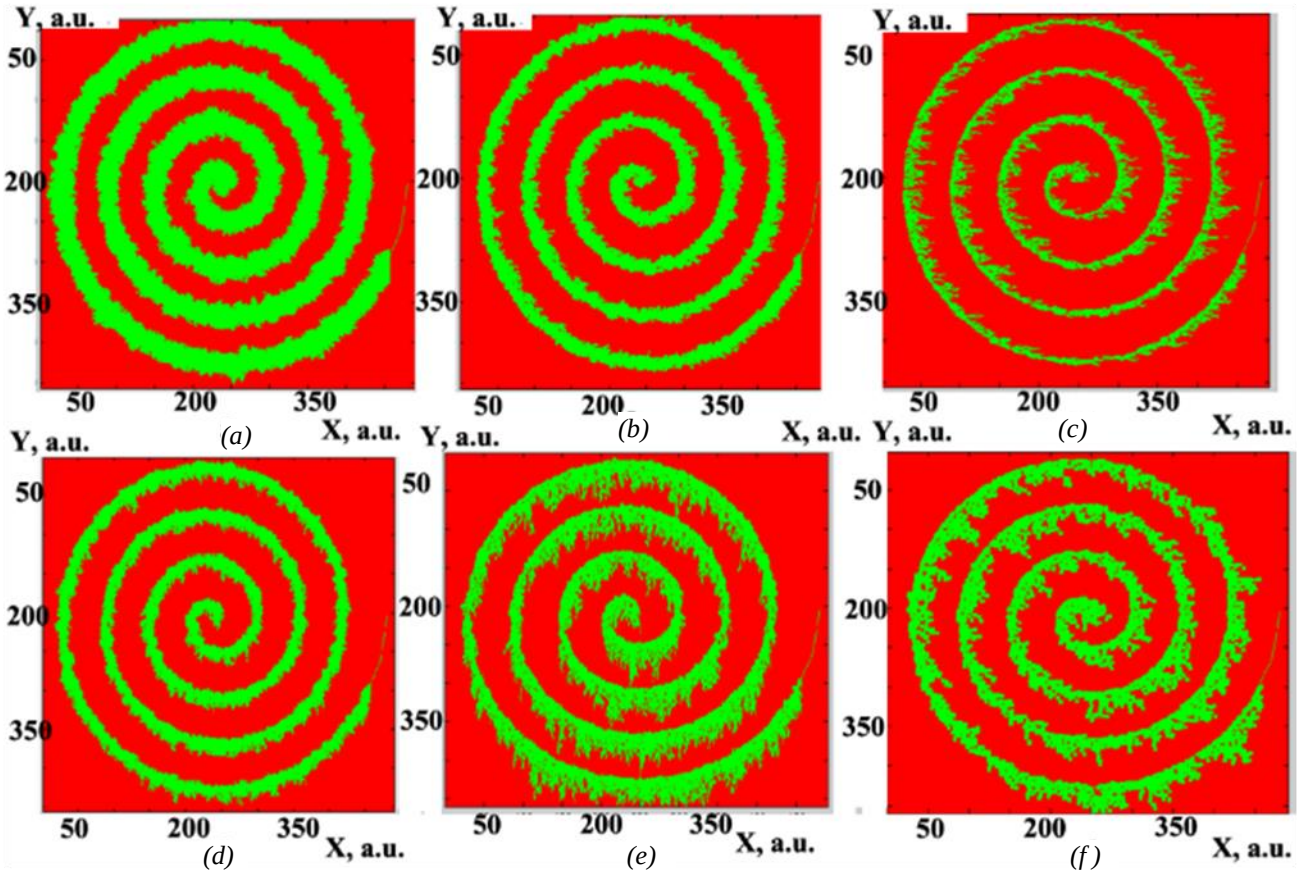

Fig. 22. Models of helicoidal structures: for initial horizontal fractal segments composed of elements with a unit length of 1 (*a*), as well as lengths of 2 (*b*) and 4 (*c*). For initial vertical lines: lengths of 2 (*d*) and 4 (*e*). For diagonal lines: length of 4 (*f*)

The modeling procedure discussed for such systems is quite versatile and could serve as an additional approach to 1D structures in various systems with a fixed nematic configuration.

4. Metal-carbon structures on a solid surface – a system of carbon nanotubes with gold atoms

In our experiment, we successfully achieved the sintering of carbon nanotubes with gold atoms using a modified form of graphite, shungite, followed by the creation of thin-layer structures on a solid surface. The sintering was conducted in a liquid environment where shungite powder was intensely mixed with a colloidal gold solution under the influence of ultrasound. The resulting system was then irradiated with laser radiation to deposit it onto a solid substrate. A series of TEM images is shown in Fig. 23.

A simulation model within the framework of the DLA approach can be used to describe this metal-carbon nanotube structure. Analysis of the transmission electron microscope images indicates that the synthesized nanotubes have a curved shape. Structures with this shape can be synthesized using a random walk model due to diffusion on the plane through random changes in the coordinates (x, y) of the moving model particles on the plane.

$$x_n = x_0 + \sum_{i=1}^{n} \gamma_i; \quad y_n = y_0 + \sum_{i=1}^{n} \delta_i,$$

where x_0, y_0 are the coordinates of the starting point of the diffusion walk, γ and δ are the horizontal and vertical steps, respectively, and n is the number of steps. The movement of a single model particle generates an individual nanotube.

In the central part of the simulation area, the effect of a laser beam with a specified relative diameter $r = \mu d$ was modeled, where μ is the scaling factor, and d is the diameter of the model particle. Then, outside the laser-affected area, the relationship was evaluated as:

$$\gamma_i = \delta_i = \sqrt{2D\tau}\, r_n \Delta_c,$$

where $D = \dfrac{k_b T}{3\pi\varepsilon d}$, D is the diffusion coefficient, k_b is the Boltzmann constant, ε is the dynamic viscosity, T is the temperature, τ is the time step, r_n is a normally distributed random number, and Δ_c is the step reduction factor: $\Delta_c = 1/r_c$, where r_c is a random integer from the interval [1, N_c], and [1, N_c] is the number of modeled nanotubes.

In the laser-affected area, the step length for both the horizontal and vertical directions was evaluated as $\alpha\gamma_i$ and $\alpha\delta_i$ respectively, where $\alpha > 1$ is the coefficient describing the acceleration of the model particle due to laser exposure.

Figure 24*a* shows an image of a model structure of a bundle of nanotubes deposited from an aqueous colloidal solution. Figure 24*b* provides an assessment of the lengths of the formed structures.

Electrophysical Characteristics. Current-voltage characteristics (IV curves) were measured using a four-probe setup [81] with an RT-70V device in a simple configuration, where the colloid we produced was deposited onto an aluminum target. Measurements were conducted in two modes: (1) “contact” mode, where one probe is in contact with the surface of the substrate and the second probe is on the deposited layer, and (2) «tunnel» contact mode, where the second probe is lifted a small distance (approximately 0.1 nm) above the surface. This setup is typical for a Schottky diode, meaning we have an *n*-type semiconductor layer on top of a metal layer.

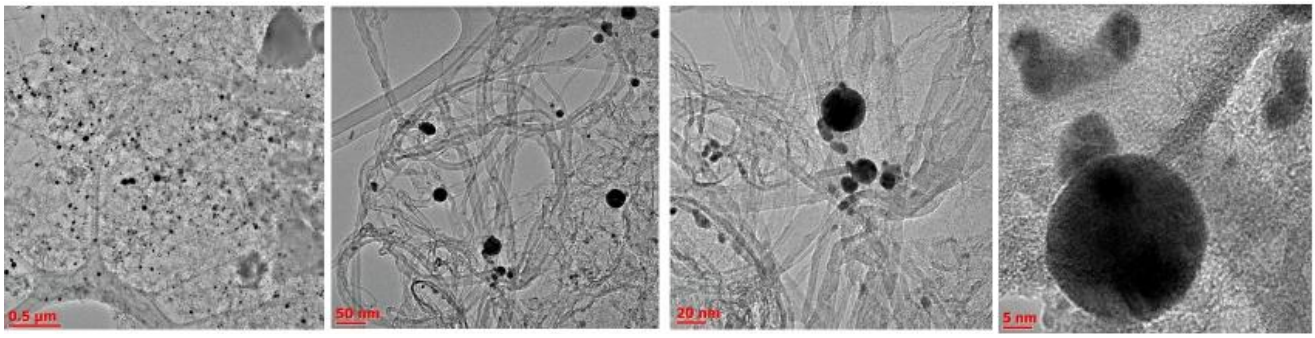

(a) *(b)* *(c)* *(d)*

Fig. 23. TEM images of a thin-film system of carbon nanotubes (elongated strands) with gold atoms (dark clustered inclusions) on a solid-state quartz substrate with shungite (general background). Images *a*–*d* correspond to different magnifications in the TEM

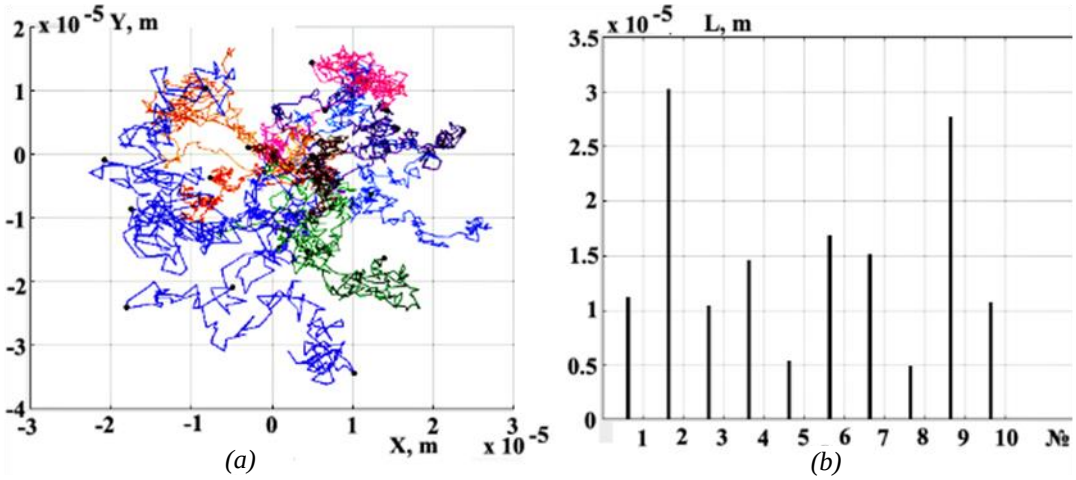

Fig. 24. Model of a nanotube bundle: the structure consists of 10 nanotubes, with model gold atoms marked by dots (*a*); histogram of the length distribution of the model nanotubes, where N is the nanotube number (*b*)

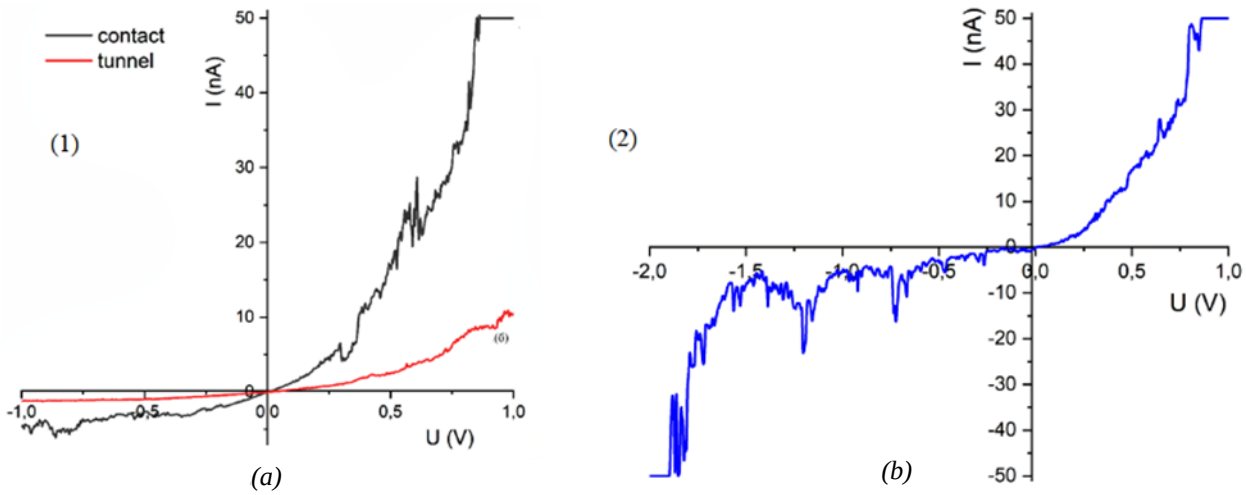

Fig. 25. (1) IV characteristics – the dependence for the two measurement configurations (see text): *a* – contact; *b* – tunnel; (2) – IV characteristics with a change in the polarity of the applied microcontacts

The voltage range parameters were [–1; 1] V, chosen because, for metal IV characteristics in this range, the behavior should remain linear. This holds true for both the contact scheme and the tunnel mode. The system was not driven to the breakdown state during reverse current measurements. The IV curves obtained for one of the samples in the two configurations mentioned are shown in Fig. 25. A significantly nonlinear behavior is observed in the IV curves. This non-ohmic behavior is fundamentally important in the development and creation of electronic systems of the trigger type using metal-carbon nanocomposites.

The increase in the effect generally depended on the topological features of the formed nanostructures – specifically, the number of dendrites/fractals, as well as the degree of their filling and connectivity within the entire system. Conductivity increased when a greater number of clusters formed in the longitudinal direction compared to the transverse direction. This fact influences the magnitude of the current jump shown in Fig. 25.

It was also found that the type of topology formed in the laser setup can be controlled and predetermined. This capability is determined by the selected characteristics of the laser radiation – such as power, beam diameter, scanning speed across the surface, and exposure time to the system. Additionally, in the structures we obtained, conductivity increased with rising temperature T according to the following relationship:

$$\sigma \sim \frac{1}{\exp(\varphi/kT)}$$

where k is the Boltzmann constant and φ is the activation energy of conductivity [17].

The dependencies obtained require separate, detailed consideration, taking into account various

factors, including the complex sintering process, where different adsorption effects on the gold atoms must be considered. These effects alter their electrophysical and physicochemical properties, including binding energy, adhesion probabilities, thermally activated efficiency, and other parameters. We will note only a few distinctive characteristics observed in the obtained dependencies (cf. [3, 34]).

First, the presence of regions with zero conductivity may indicate the emergence of a bandgap similar to that in semiconductors, meaning that in such structures, the gold atoms undergo a transition from metallic conductivity to semiconducting behavior. This is a non-trivial process.

Second, the observed jumps in measured tunneling conductivity suggest the influence of topological factors, particularly the emergence of excess charge states on the surface of nanostructures depending on their shape and size. Here, processes such as resonant electron transitions at contacts of different polarity and mutual polarization effects between neighboring nanoparticles and their surroundings may play a decisive role. This alters the characteristics of the thermally activated effects responsible for the sample's conductivity.

The physics of isolated gold nanoparticles combined with carbon nanotubes, especially in a thin-film structure with shungite, represents one of the promising areas in modern topological electrophysics of metal-carbon composites, with applications in various nanoelectronics tasks. Even more interesting are the fractal structures synthesized in the laser experiment, which can be controllably implemented.

In this context, it is useful to briefly consider a model of electric field enhancement on fractal structures, such as those shown in Fig. 3, which, in the simplest model representation, consist of elements in the form of long branches with fractal segments at their ends. The electric field intensity at the tip of an individual fractal structure can be expressed as

$$E(r) = \frac{1}{4\pi\varepsilon_0}\frac{q}{R^3}r,$$

where R is the radius of the tip. Let's assume the tip can be approximated by a sphere with such a radius R. Then, the field intensity at the tip is estimated as $E_b(R) \sim \frac{1}{R^2}$. Regarding the enhancement G at the end of an isolated tip, it can be calculated using the ratio $G = E_b/E_f$, where $E_f \sim \frac{1}{R_f^2}$, and R_f is the radius of the minimum coverage circle in the calculation procedure used. In experiments, this corresponds to natural averaging over a spatial area on the sample's surface when measuring the electrophysical parameters in each local area using a microcontact with a certain finite cross-section (which determines the technical limitation on the local measurement accuracy).

To estimate the relative enhancement in structures like those in Fig. 3, within the considered framework, it is necessary to adopt a numerical model of the fractal object with specific characteristics. Our analysis shows that effective enhancement can be achieved for the following structural features of the fractal with the parameters: the relative diameter of the minimum coverage circle should be, in arbitrary units, 16 a. u., for example, with the fractal object having 8 long branches, 34 ends, and an average tip radius of 0.5 a. u. Then, the localized conditional enhancement at the end of an individual long branch would theoretically be 256, while the total integral enhancement over the calculation area, as measured in the experiment with the finite coverage area of the structure, is estimated to increase the electric field strength by 5 orders of magnitude (for the specified parameters, this amounts to $8.7 \cdot 10^4$).

Thus, we have demonstrated that in model samples, within the proposed approximation, it is possible to achieve relative enhancement of the electric field by several orders of magnitude, considering the entire perimeter of the branched fractal figure within a specific coverage area when measured with a microcontact. This effect is similar to the well-known phenomenon of giant Raman scattering (SERS) enhancement on rough surfaces, used, in particular, for detecting extremely low concentrations of dyes on such surfaces (cf. [4, 8, 9, 15, 80]).

5. Laser ablation of diamond surfaces and defect structures in them

Carbon composites, similar to systems with carbon nanotubes, can also include diamond-like materials, in which graphitization processes occur, determining their electrophysical characteristics. Absorption spectra for different carbon materials are well known and are shown in Fig. 26 [81]. As seen, diamond exhibits a narrow absorption peak around 200 nm compared to other diamond-like forms shown in the same figure.

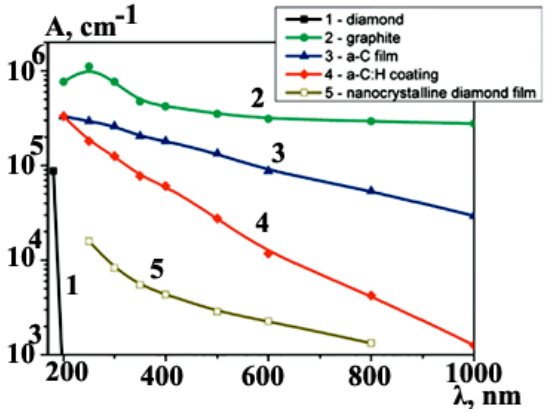

Fig. 26. Dependence of the optical absorption coefficient (A, in cm^{-1}) on the wavelength of laser radiation λ (in nm) for various carbon nanomaterials. The peak around 200 nm corresponds to diamond

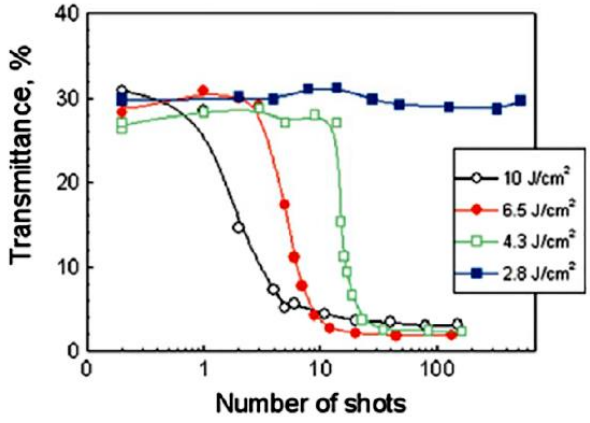

Fig. 27. Dependence of the optical transmittance coefficient of diamond on the energy density of laser irradiation and the number of laser pulses applied

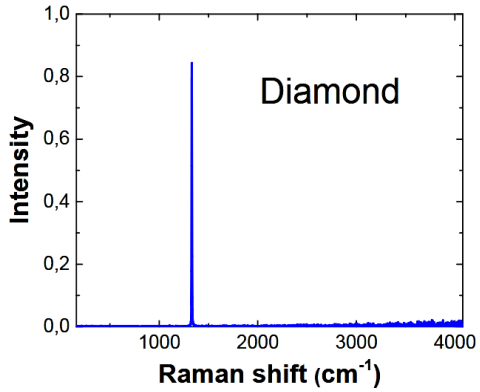

Fig. 28. Raman scattering spectrum for the surface of a diamond sample after laser ablation with graphitization of the irradiated area

For diamond, under the influence of picosecond-duration pulsed laser radiation, its transmittance is highly dependent on the laser irradiation mode (number of pulses, energy density) – Fig. 27 [81]. It can be seen that at high laser energy densities, the transmittance coefficient sharply decreases even with a small number of irradiation pulses.

This effect is associated with the graphitization of diamond, which is confirmed by the Raman scattering spectrum shown in Fig. 28, following surface laser ablation of the diamond sample [82].

The thermally induced phase transformation process from diamond to graphite begins at the surface and gradually spreads deeper into the diamond crystal. Using pulsed laser irradiation [83–86] allows the localization of the diamond-to-graphite transformation process within a submicron region, which can be moved inside the crystal in any desired direction by appropriately focusing the laser beam within the diamond sample. Ultimately, this technology enables the creation of three-dimensional conductive microstructures of various shapes within the diamond volume.

To assess the accuracy of the modeling, it is easy to compare the fractal dimensions in the images of models with those in real samples using the methodology described in Section 2.

The proposed model for analyzing the graphitization process during the development of a diffusion process, considered within the framework of a cellular automaton algorithm, allows for an evaluation of the influence of experimental laser synthesis control parameters on the graphitization effect in diamond. The connection between the model and these experimental parameters arises through the value of the occupancy probability (s) of a cell in the calculation area as a function of the relative temperature. For example, studies of the structure of graphitized areas obtained through pulsed laser exposure indicate that one of the controlling parameters is pulse duration, an increase of which leads to an increase in the critical speed of the laser beam focus movement within the sample. This effect is accompanied by the appearance of discontinuities.

Figure 29 shows models of graphitization areas constructed based on the diffusion model, where the graphitization area began to spread from different starting objects: from a straight line (Fig. 29*a*); from a system of points (Fig. 29*b*); from a system of fractal cracks (Fig. 29*c*), constructed using DLA approximation (Fig. 29*d* – final structure). In the center of the calculation area for Figs. 29*a* and 29*b*, the occupancy probability s (which determined the growth of the graphitization structure) was set to be twice as high as in other parts. This allowed for the creation of structures with a predetermined growth direction.

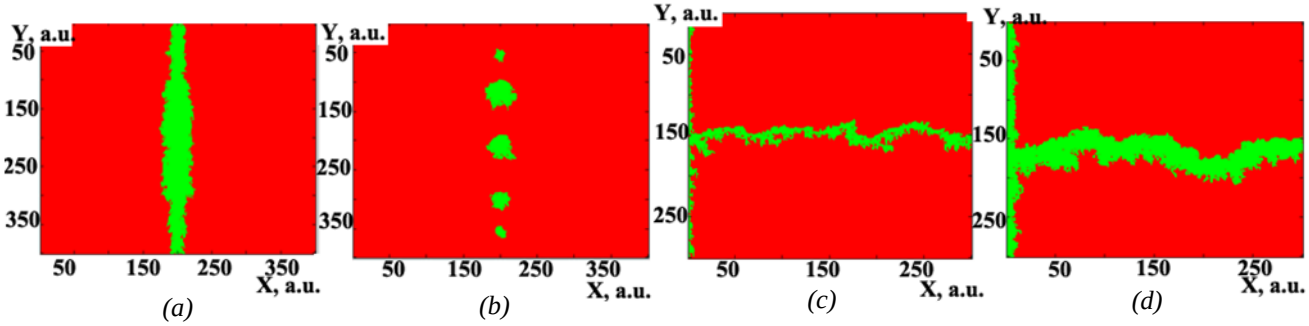

Fig. 29. Simulation results of the graphitized area for different initial structures with an occupancy probability of s = 0.0073: a straight line (*a*); a system of points (*b*); DLA model of a fractal crack system (*c*); the final structure of the graphitized area corresponding to the initial fractal crack system (*d*)

Similar but more branched and heterogeneous structures can also be generated within the DLA model. Figure 30 shows such models considering various initial conditions. The implementation of random walks during the iterative process in the DLA model allows the generation of structures with a more pronounced desired growth direction. For example, the models shown in Fig. 30 exhibit predominant growth toward the right.

In addition to surface laser ablation of diamond crystals, bulk transformation in a laser field is also possible [85, 87, 84]. These 3D microstructures within the diamond can naturally be created by moving the sample through the focus of the laser beam (see [86]). Raman microspectroscopy has shown that the laser-modified material is a mixture of amorphous and graphitic structures. This is further confirmed by the measurement of the electrical conductivity of such samples [88].

However, a complete transformation of bulk sp^3-diamond into sp^2-carbon structure, during this laser-induced phase transition, is hindered by the emergence of compressive and tensile stresses due to the significant density difference between these two allotropes of carbon. As a result, the resulting electrically conductive structures typically consist of numerous micro- and nanoscale sp^2-carbon inclusions within a sp^3-diamond matrix. According to [88], this occurs via a percolation mechanism.

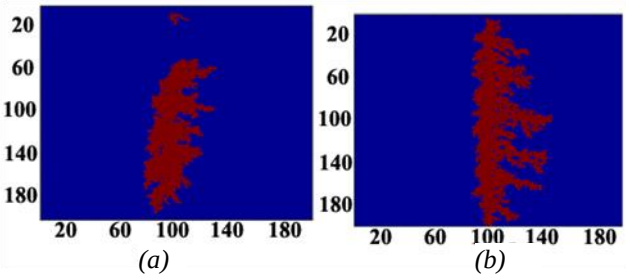

Fig. 30. DLA model results of the graphitized area for different initial structures with s = 0.1: two regions (*a*); a straight line (*b*)

Furthermore, one of the allotropic modifications of diamond is the natural mineral lonsdaleite (hexagonal diamond). For a long time, it was believed that lonsdaleite, which has also been synthesized artificially, could only exist in diamonds as defects and twins [89]. However, this involves different twinning mechanisms, particularly the shifting and displacement of layers in the martensitic class.

Indeed, it has been found that the crystal structure of lonsdaleite is hexagonal with lattice parameters a = 2.52 Å, c = 4.12 Å [89]. The difference between diamond and lonsdaleite lies in the packing sequence of the layers. The diamond crystal lattice (denoted as 3C) has a layer sequence indexed by the crystal lattice elements ABCABC [89], while the lonsdaleite crystal lattice (denoted as 2H) has a layer sequence of ABAB. Packing defects that arise in the diamond lattice during growth contain lonsdaleite interlayers. The theoretical density of lonsdaleite is the same as that of diamond (3.51 g·cm^{-3}).

Figure 31 shows a fragment of a diamond crystal containing numerous defects [89], with the zone axis [110] visible. Two systems of {111} planes with an interplanar distance of 0.206 nm can be seen. The characteristic planes (1-11) and (1-1-1) of diamond form a 70° angle. Dashed black lines indicate structural changes caused by packing defects. Additionally, incoherent twin boundaries are marked with asterisks in Fig. 31. The difference between such boundaries and traditional twins is the lack of a clear boundary, instead displaying broken lines marked with asterisks. Rectangles denote fragments of the diamond sample with a lonsdaleite lattice. The rectangular fragments of lonsdaleite are rotated by 70°. In such a structure, they could be formed through a twinning mechanism via mirror reflection from a plane symmetrically located between adjacent {111} planes in the diamond crystal. Considering the [110] zone axis as the mirror reflection plane, it could be

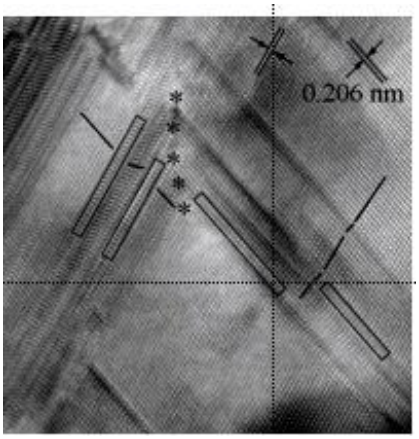

Fig. 31. Structure of Diamond-Lonsdaleite

the (3-308) plane in hexagonal close-packed (HCP) coordinates, which corresponds to (101) or (-3304) in face-centered cubic (FCC) coordinates. Indeed, they belong to the [110] HCP zone axis and form angles of 35.30° and 35.25° with (001)-HCP and (-3302)-FCC, respectively. The established twinning planes (3-308) HCP and (-3304) HCP are typically not characteristic of crystals with an HCP lattice structure.

The zone axis [110] is shown. Two systems of {111} planes are visible with an interplanar distance of 0.206 nm. Dashed black lines indicate changes in structure caused by packing defects. Rectangles denote fragments of lonsdaleite, and asterisks mark incoherent twin boundaries.

In addition to individual layers of lonsdaleite in diamond packing, relatively large lonsdaleite fragments are sometimes observed [89]. Besides lonsdaleite, 4H polytypes (repeated layers of CBCA…; known as 4H polytypes in diamond) and 6H (layer sequence ABCACB…) were also discovered.

These structures hold great promise for creating semiconductor materials with controllable electronic states and achieving specific electrophysical characteristics in various conditions.

Furthermore, during the synthesis of nanotwinned topological polycrystalline bulk materials from onion-like structures, nanodiamonds with twinned structures were obtained from isolated onion-like blocks, for which potassium chloride particles were used [90]. Under conditions of high pressure and high temperature, these were observed to transform into martensite.

Reference [90] also argues that the properties of homoepitaxial diamond films (111) are influenced by the presence of twins, as well as packing defects, impurities, and dislocations.

Thus, various diamond-like structures, especially those with twinning, represent a distinct branch of modern diamond nanotechnology (cf. [3]). Overall, twinning theory is essential for applications; it requires both microscopic and macroscopic examination, which, however, falls outside the scope of this article.

6. Conclusion

In this partially review-based article, we examined the modeling of various topological configurations in metal-carbon nanocomposites with carbon nanotubes based on our results. The review focused on the potential of digital materials science technologies to control the electrophysical characteristics of these topologically synthesized structures in laser experiments.

These laser methods are relatively simple and inexpensive (even when using femtosecond laser irradiation that develops nonequilibrium nonlinear effects in the target) compared to traditional methods of growing nanofilms. In particular, this includes comparing laser methods with the synthesis of semiconductor compounds and hybrid porous nanomaterials, including high-entropy alloys. In laser schemes, this can be done with virtually no restrictions on composition or thickness, down to a few nanometers, unlike the conventional methods of molecular beam epitaxy and metal-organic chemical vapor deposition.

Moreover, by controlling various laser modes, it is possible not only to create topological systems of a specific configuration but also to manage undesirable processes such as aggregation, dispersion, and fragmentation of nanoclusters (which can also be influenced by temperature factors), and to control their mobility during the synthesis of nanostructures with the desired concentration of components.

Despite the initial development of non-stationary nonequilibrium processes during their formation, these objects can remain stable in terms of stabilizing quasi-equilibrium quantum states. This is due to their topological features, which, for example, lead to changes in thermophysical and thermodynamic characteristics during phase transitions, making them irreversible or at least giving them hysteresis. It is important to note that the deformation process of an object's structure (especially in crystal lattices and/or 2D structures) can be likened to the effect of magnetic fields.

The discussed effects and the possibility of controlling them with laser methods hold great promise for the development of micro-nanoelectronics elements and systems based on new physical principles. In the near future, significant experimental results are expected in this area,

including the identification of trends in the synthesis of high-temperature states in superconductivity within topological structures of different classes.

7. Funding

This research was conducted as part of the state assignment to VSU “Development of methods for surface laser modification of synthetic diamond films and wide-bandgap compositions based on it for controlling the optical and electrophysical properties of structured materials” (FZUN-2023-0003).

8. Conflict of interests

The authors declare no conflict of interest.

References

1. Kresin VZ, Ovchinnikov YuN. «'Giant» strengthening of superconducting pairing in metallic nanoclusters: large enhancement of Tc and potential for room-temperature superconductivity. *Uspekhi fizicheskikh nauk = Physics-Uspekhi*. 2008;51:427-435. DOI:10.1070/PU2008v051n05ABEH006531

2. Troyan IA, Semenok DV, Ivanova AG, Kvashnin AG, et al. High-temperature superconductivity in hydrides. *Uspekhi fizicheskikh nauk = Physics-Uspekhi.* 2022;65: 748-761. DOI:10.3367/UFNe.2021.05.039187

3. Trahtenberg LI, Melnikov MYa. *Metal/ semiconductor containing nanocomposites.* Moscow: Tehnosfera; 2016. 624 p. (In Russ.)

4. Garnov SV, Abramov DV, Bukharov DN, Khudaiberganov TA, et al. Electrophysics of carbon 1D structures obtained in a laser experiment: models and demonstration. *Uspekhi fizicheskikh nauk = Physics-Uspekhi*. 2024;67:109-128. DOI:10.3367/UFNe.2023.12.039620

5. Bukharov DN, Kucherik AO, Arakelian SM. Nanocluster fractal electrical conductivity in thin films on a solid surface: dimensional models of different configurations and demonstration of results in a laser experiment. *Journal of Advanced Materials and Technology*. 2023;8(3):227-251. DOI:10.17277/jamt.2023.03.pp.227-251

6. Kozhushner MA, Bodneva VL, Trahtenberg LI. Theory of sensory effect in detecting reducing gases. *Zhurnal fizicheskoy khimii= Russian Journal of Physical Chemistry A.* 2012;86(6):1397-1404. (In Russ.)

7. Arakelyan SM, Buharov DN, Kucherik AO, Hudajberganov TA. Dynamic and quantum effects in cluster low-dimensional multilayer solid-state nanostructures for the element base of micro- and nanoelectronics. *Izvestiya Rossiyskoy akademii nauk. Seriya fizicheskaya = Bulletin of the Russian Academy of Sciences: Physics*. 2022;86(6):834-840. (In Russ.)

8. Belysheva TV, Gatin AK, Grishin MV, Ikim MI, et al. Structure and physicochemical properties of nanostructured films of metal oxides - a sensitive layer of gas sensors. *Khimicheskaya fizika = Russian Journal of Physical Chemistry B*. 2015;34(9):56-67. DOI:10.7868/S0207401X15090046 (In Russ.)

9. Kulbachinsky VA. *Physics of nanosystems*. Moscow: Fizmatlit; 2021. 768 p. (In Russ.)

10. Zuev DA, Lotin AA, Novodvorsky OA, Lebedev FV, et al. Pulsed laser deposition of ITO thin films and their characteristics. *Fizika i tekhnika poluprovodnikov = Semiconductors*. 2012;46(3):425-429. (In Russ.)

11. Kozhushner MA, Trakhtenberg LI. Conductivity of composites containing ferromagnetic nanoparticles. The role of the magnetic field. *Zhurnal eksperimental'noy i teoreticheskoy fiziki = Journal of Experimental and Theoretical Physics*. 2010;138(6):1144-1152. (In Russ.)

12. Khorkov K, Kochuev D, Chkalov R, Prokoshev V, Arakelian S. Nonlinear dynamic processes in laser-induced transitions to low-dimensional carbon nanostructures in bulk graphite unit. *New Trends in Nonlinear Dynamics – Proceedings of the 1st International Nonlinear Dynamics Conference, NODYCON 2019: 1, Rome, 17-20 February 2019*. Springer Nature: Switzerland; 2020. p.131-140.

13. Gehrke MN, Bukharov DN, Istratov AV, Novikova OA, et al. Study of the structure and electrical conductivity of thin bimetallic granular films. *Izvestiya Rossiyskoy akademii nauk. Seriya fizicheskaya = Bulletin of the Russian Academy of Sciences: Physics*. 2017;81(12):1572-1575. (In Russ.)

14. Trakhtenberg LI, Gerasimov GN, Gromov VF, Belysheva TV, Ilegbusi OJ. Effect of composition on sensing properties of SnO_2 + In_2O_3 mixed nano-structured films. *Sensors and Actuators B: Chemical.* 2012;169:32-38. DOI:10.1016/j.snb.2012.01.064

15. Arakelyan SM, Kucherik AO, Prokoshev VG, Rau VG, Sergeev AG. *Introduction to femtonano-photonics. Fundamentals and laser methods for controlled production and diagnostics of nanostructured materials*. Moscow: Logos; 2015. 744 p. (In Russ.)

16. Marukovich EH, Stetsenko VYu, Stetsenko AV. Nanostructured crystallization of metals. *Lit'ye i metallurgiya*. 2021;2:23-26. (In Russ.)

17. Kavokin A, Kutrovskaya S, Kucherik A, Osipov A, et al. The crossover between tunnel and hopping conductivity in granulated films of noble metals. *Superlattices and Microstructures*. 2017;111:335-339. DOI:10.1016/j.spmi.2017.06.050

18. Eletsky AV, Knizhnik AA, Potapkin BV, Kenny HM. Electrical characteristics of polymer composites containing carbon nanotubes. *Uspekhi fizicheskikh nauk = Physics-Uspekhi*. 2015;185:225-270. DOI:10.3367/UFNr.0185.201503a.0225 (In Russ.)

19. Bauhofer W, Kovacs JZ. A review and analysis of electrical percolation in carbon nanotube polymer composites. *Composites Science and Technology*. 2009; 69(10):1486-1498. DOI:10.1016/j.compscitech.2008.06.018

20. Eletsky AV. Transport properties of carbon nanotubes. *Uspekhi fizicheskikh nauk = Physics-Uspekhi.* 2009;52(3):209-224. DOI:10.3367/UFNr.0179.200903a.0225 (In Russ.)

21. Cardoso P, Silva J, Paleo AJ, Van Hattum FWJ, et al. The dominant role of tunneling in the conductivity of

carbon nanofiber epoxy composites. *Physica Status Solidi (A)*. 2010;207(2):407-410. DOI:10.1002/pssa.200925334

22. Salvato M, Cirillo M, Lucci M, Orlanducci S, et al. Charge transport and tunneling in single-walled carbon nanotube bundles. *Physical Review Letters*. 2008;101(24): 246804. DOI:10.1103/PhysRevLett.101.246804

23. Malinetsky GG, Potapov AB, Podlazov AV. *Nonlinear dynamics. Approaches, results, hopes*. Moscow: URSS; 2016. 280 p. (In Russ.)

24. Grimaldi C, Mionić M, Gaal R, Forró L, Magrez A. Electrical conductivity of multi-walled carbon nanotubes-SU8 epoxy composites. *Applied Physics Letters*. 2013;102(22):223114. DOI:10.1063/1.4809923

25. Arakelian SM, Bucharov DN, Emel'yanov VI, Zimin SP, et al. Bimodal ensemble of nanoparticles on the surface of epitaxial lead telluride films under continuous laser radiation. *Journal of Surface Investigation. X-ray, Synchrotron and Neutron Techniques*. 2015;9(6):1156-1163. DOI:10.1134/S1027451015060063

26. Sarychev AK, Shalaev VM. *Electrodynamics of metamaterials*. Moscow: Scientific world; 2011. 224 p. (In Russ.)

27. Celzard A, McRae E, Deleuze C, Dufort M, et al. Critical concentration in percolating systems containing a high-aspect-ratio filler. *Physical Review B*. 1996;53(10): 6209-6214. DOI:10.1103/PhysRevB.53.6209

28. Hu N, Masuda Z, Yamamoto G, Fukunaga H, Hashida T, Qiu J. Effect of fabrication process on electrical properties of polymer/multi-wall carbon nanotube nanocomposites. *Composites Part A: Applied Science and Manufacturing*. 2008;39(5):893-903. DOI:10.1016/ j.compositesa.2008.01.002

29. Charlier J-C, Blase X, Roche S. Electronic and transport properties of nanotubes. *Reviews of Modern Physics*. 2007;79(2):677-732. DOI:10.1103/RevModPhys. 79.677

30. Terenzi A, Natali M, Petrucci R, Rallini M, et al. Analysis and simulation of the electrical properties of CNTs/epoxy nanocomposites for high performance composite matrices. *Polymer Composites*. 2015;38(1): 105115. DOI:10.1002/pc.23565

31. Penazzi G, Carlsson JM, Diedrich C, Olf G, et al. Atomistic modeling of charge transport across a carbon nanotube–polyethylene junction. *The Journal of Physical Chemistry C*. 2013;117(16):8020-8027. DOI:10.1021/ jp312381k

32. Pavlushin A, Konogorova DV. Crystallogenetic prerequisites for the emergence of a unique form of diamond "Matryoshka" – the effect of capture of a diamond inclusion by a twin of diamond crystals. *Geohimiya*. 2023;68(3):271-284. DOI:10.31857/ S001675252303010X (In Russ.)

33. Khorkov KS, Prokoshev VG, Arakelian SM. Laser-induced methods for obtaining carbon nanomaterials in liquid nitrogen under femtosecond radiation. *Journal of Advanced Materials and Technologies*. 2021;6(2):101-112. DOI:10.17277/jamt.2021.02.pp.101-112

34. Mishchenko SV, Tkachev AG. *Carbon nanomaterials. Production, properties, application*. Moscow: Mechanical Engineering; 2008. 320 p. (In Russ.)

35. Ellert OG, Tsodikov MV, Nikolaev SA, Novotortsev VM. Bimetallic nanoalloys in heterogeneous catalysis of industrially important reactions: synergetic effects and structural organization of the active components. *Russian Chemical Reviews*. 2014;83(8):718-732. DOI:10.1070/RC2014v083n08ABEH004432

36. Lu W, Chou T-W, Thostenson ET. A three-dimensional model of electrical percolation thresholds in carbon nanotube-based composites. *Applied Physics Letters*. 2010;96(22):223106. DOI:10.1063/1.3443731

37. Logakis E, Pandis Ch, Peoglos V, Pissis P, et al. Electrical/dielectric properties and conduction mechanism in melt processed polyamide/multi-walled carbon nanotubes composites. *Polymer*. 2009;50(21):5103-5111. DOI:10.1016/j.polymer.2009.08.038

38. Yu Y, Song G, Sun L. Determinant role of tunneling resistance in electrical conductivity of polymer composites reinforced by well dispersed carbon nanotubes. *Journal of Applied Physics*. 2010;108(8):084319. DOI:10.1063/1.3499628

39. Antipov AA, Arakelyan SM, Bukharov DN, Kutrovskaya SV, et al. Laser synthesis of micro-nanoparticles in liquid media. *Khimicheskaya fizika i mezoskopiya*. 2012;14(3):401-407. (In Russ.)

40. Gonsales R, Woods R, Eddins S. *Digital image processing in the MATLAB*. Moscow: Tekhnosfera; 2006. 616 p. (In Russ.)

41. Gonzato G. A practical implementation of the box counting algorithm. *Computers & Geosciences*. 1998; 24(1):95-100. DOI:10.1016/S0098-3004(97)00137-4

42. Ryzhikova YuV, Ryzhikov SB. Fractal properties of self-organizing dendritic structures. *Uchenye zapiski fizicheskogo fakul'teta Moskovskogo Universiteta*. 2018;(5):1850401. (In Russ.)

43. Mroczka J, Woźniak M, Onofri FRA. Algorithms and methods for analysis of the optical structure factor of fractal aggregates. *Metrology and Measurement Systems*. 2012;19(3):359-370. DOI:10.2478/v10178-012-0039-2

44. Lobanov AI. Models of cellular automata. *Komp'yuternyye issledovaniya i modelirovaniye*. 2010;2(3):273-293. (In Russ.)

45. Samarskiy AA, Vabishchevich PN. *Computational heat transfer*. Moscow: URSS; 2020. 784 p. (In Russ.)

46. Bukharov DN. Thermal diffusion model of a system of lead telluride nanoclusters. *Nanoelectronics, nanophotonics and nonlinear physics. Collection of works of the XVIII All-Russian Conference of Young Scientists. Saratov*: "Techno-Décor" publ. house; 2023. 227 p. (In Russ.)

47. Nechaev, YS. On the nature, kinetics and limiting values of hydrogen sorption by carbon nanostructures. *Uspekh ifizicheskikh nauk = Physics-Uspekhi*. 2006;176(6):581-610. DOI:10.3367/UFNr.0176.200606b. 0581 (In Russ.)

48. Prudnikov M, Linnik AI, Shalaev RV, Rumyantsev VV, et al. Features of the formation and modification of nanostructured carbon nitride films. *Nanosistemy: fizika, khimiya, matematika*. 2012;3(6):134-145. (In Russ.)

49. Ampilova NB. Algorithms for fractal image analysis. *Komp'yuternyye instrumenty v obrazovanii*. 2012;(2):19-24. (In Russ.)

50. Bukharov DN, Arakelyan SM, Kucherik AO, Novikova OA, Samyshkin VD. Mathematical modeling of the structure and optical properties of the fractal island metal nanofilm. *Journal of Physics: Conference Series*. 2020;1439(1):012050. DOI:10.1088/1742-6596/1439/1/012050

51. Belankov AB, Stolbov VYu. Application of cellular automata for modeling the microstructure of a material during crystallization. *Sibirskiy Zhurnal industrial'noy matematiki = Journal of Applied and Industrial Mathematics.* 2005;8(2(22)):12-19. (In Russ.)

52. Dong X, Oganov AR, Cui H, Zhou X-F, Wang H-T. Electronegativity and chemical hardness of elements under pressure. *Proceedings of the National Academy of Sciences*. 2022;119(10):e2117416119. DOI:10.1073/pnas.2117416119

53. Berghoff D, Bühler J, Bonn M, Leitenstorfer A, et al. Low-field onset of Wannier-Stark localization in a polycrystalline hybrid organic inorganic perovskite. *Nature Communications*. 2021;12(1):5719. DOI:10.1038/s41467-021-26021-4

54. Frey P, Rachel S. Realization of a discrete time crystal on 57 qubits of a quantum computer. *Science Advances*. 2022;8(9):eabm7652. DOI:10.1126/sciadv.abm7652

55. Sun L-H, Ounaies Z, Gao X-L, Whalen CA, Yang Z-G. Preparation, characterization, and modeling of carbon nanofiber/epoxy nanocomposites. *Journal of Nanomaterials*. 2011;2011:1-8. DOI:10.1155/2011/307589

56. Magomedov MN. On the baric fragmentation of a crystal. *Physics of the Solid State*. 2003;45(5):908-910. DOI:10.1134/1.1575343

57. Arakelian S, Kutrovskaya S, Kucherik A, Osipov A, et al. Laser-induced synthesis of nanostructured metal-carbon clusters and complexes. *Optical and Quantum Electronics*. 2016;48(11):505. DOI:10.1007/s11082-016-0776-7

58. Cannella CB, Goldman N. Carbyne fiber synthesis within evaporating metallic liquid carbon. *The Journal of Physical Chemistry C*. 2015;119(37):21605-21611. DOI:10.1021/acs.jpcc.5b03781

59. Kutrovskaya SV, Arakelian SM, Kucherik AO, Osipov AV, Garnov SV. Long linear carbon chain – laser-induced structures and possible applications. *Laser Physics.* 2019;29(8):085901. DOI:10.1088/1555-6611/ab183a

60. Kucherik AO, Arakelyan SM, Garnov SV, Kutrovskaya SV, et al. Two-step laser-induced synthesis of linear carbon chains. *Kvantovaya elektronika= Quantum Electronics*. 2016;46(7):627-633. (In Russ.)

61. Landau LD, Lifshits EM. *Theoretical physics. Statistical physics*. Moscow: Fizmatlit; 2002. 616 p. (In Russ.)

62. Kutrovskaya S, Samyshkin V, Lelekova A, Povolotskiy A, et al. Field-Induced assembly of *sp*-sp^2 carbon sponges. *Nanomaterials*. 2021;11(3):763. DOI:10.3390/nano11030763

63. Wang Q, Shen Y, Pan B, Hao Y, et al. Strong interplay between stripe spin fluctuations, nematicity and superconductivity in FeSe. *Nature Materials*. 2016;15(2):159-163. DOI:10.1038/nmat4492

64. Kucherik A, Arakelian S, Vartanyan T, Kutrovskaya S, et al. Laser-induced synthesis of metal – carbon materials for implementing surface-enhanced Raman scattering. *Optics and Spectroscopy*. 2016;121(2): 263-270. DOI:10.1134/S0030400X16080105

65. Downer MC, Ahn H, Reitze DH, Wang XY. Dielectric function and electrical resistivity of liquid carbon determined by femtosecond spectroscopy. *International Journal of Thermophysics*. 1993;14(3):361-370. DOI:10.1007/BF00566036

66. Arakelian SM, Kucherik AO, Khudaberganov TA, Bukharov DN, et al. Nanophysics in laser-induced cluster systems: topological quantum states in electrical conductivity and features of optical spectra – theory and experiment for dimensional effects. *Optical and Quantum Electronics*. 2020;52(4):202. DOI:10.1007/s11082-020-02308-6

67. Kucherik AO, Osipov AV, Arakelian SM, Garnov SV, et al. The laser-assisted synthesis of linear carbon chains stabilized by noble metal particle. *Journal of Physics: Conference Series*. 2019;1164:012006. DOI:10.1088/1742-6596/1164/1/012006

68. Forgerini FL, Marchiori R. A brief review of mathematical models of thin film growth and surfaces: A possible route to avoid defects in stents. *Biomatter*. 2014;4(1):e28871. DOI:10.4161/biom.28871

69. Bukharov DN, Kucherik AO, Arakelyan SM, Lotin AA. Modeling of a profile of a PbTe semiconductor nanofilm. *Journal of Physics: Conference Series*. 2019; 1331(1):012002. DOI:10.1088/1742-6596/1331/1/012002

70. Family F, Vicsek T. Scaling of the active zone in the Eden process on percolation networks and the ballistic deposition model. *Journal of Physics A: Mathematical and General*. 1985;18(2):L75-L81. DOI:10.1088/0305-4470. 18.2.005

71. Moskalev PV. Analysis of the structure of a percolation cluster. *Zhurnal tekhnicheskoy fiziki = Technical Physics.* 2009;79(6):1-7. (In Russ.)

72. Kucherik A, Samyshkin V, Prusov E, Osipov A, et al. Formation of fractal dendrites by laser-induced melting of aluminum alloys. *Nanomaterials*. 2021;11(4):1043. DOI:10.3390/nano11041043

73. Sander LM. Diffusion-limited aggregation: A kinetic critical phenomenon. *Contemporary Physics*. 2000;41(4):203-218. DOI:10.1080/001075100409698

74. Jagota M, Tansu N. Conductivity of nanowire arrays under random and ordered orientation configurations. *Scientific Reports*. 2015;5(1):10219. DOI:10.1038/srep10219

75. Chu ChSh. Computer modeling of thin film growth processes during thermal vacuum deposition. *Izvestiya Vuzov Rossii. Radioelektronika*. 2016;6:22-31. (In Russ.)

76. Kuzmicheva GM. Nanosized systems with titanium (IV) oxides. Receipt. Characterization. Properties. *Tonkiye khimicheskiye tekhnologii*. 2015;10(6):5-36. (In Russ.)

77. Savin AV, Sakovich RA, Mazo MA. Using spiral chain models for study of nanoscroll structures. *Physical Review B*. 2018;97(16):165436. DOI:10.1103.PhysRevB.97.165436

78. Kulagin AE, Shapovalov AV. Analytical description of the diffusion in a cellular automaton with the Margolus neighbourhood in terms of the two-dimensional Markov chain. *Mathematics*. 2023;11(3):584. DOI:10.3390.math11030584

79. Bukharov DN, Skryabin IO, Arakelyan SM. Model of the microscroll structure. *Journal of Physics: Conference Series*. 2019;1331(1):012019. DOI:10.1088.1742-6596.1331.1.012019

80. Burlakov RB, Kovivchak VS. On the issue of measuring the resistivity of conductive layers using the four-probe method. *Vestnik Omskogo Universiteta*. 2014;2(72):59-68.(In Russ.)

81. Apostolova T, Kurylo V, Gnilitskyi I. Ultrafast laser processing of diamond materials: A Review. *Frontiers in Physics*. 2021;9:650280. DOI:10.3389/fphy.2021.650280

82. Tikhomirov S, Kimstach T. Raman spectroscopy – a promising method for studying carbon nanomaterials. *Analitika*. 2011;(6):28-32. (In Russ.)

83. Shimizu M, Shimotsuma Y, Sakakura M, Yuasa T, et al. Periodic metallo-dielectric structure in diamond. *Optics Express*. 2009;17(1):46-54. DOI:10.1364/OE.17.000046

84. Kononenko TV, Komlenok MS, Pashinin VP, Pimenov SM, et al. Femtosecond laser microstructuring in the bulk of diamond. *Diamond and Related Materials*. 2009;18(2-3):196-199. DOI:10.1016/j.diamond.2008.07.014

85. Kononenko TV, Konov VI, Pimenov SM, Rossukanyi NM, et al. Three-dimensional laser writing in diamond bulk. *Diamond and Related Materials*. 2011;20(2):264-268. DOI:10.1016/j.diamond.2010.12.013

86. Sun B, Salter PS, Booth MJ. High conductivity micro-wires in diamond following arbitrary paths. *Applied Physics Letters*. 2014;105(23):231105. DOI:10.1063/1.4902998

87. Shimotsuma Y. Three-dimensional nanostructuring of transparent materials by the femtosecond laser irradiation. *Journal of Laser Micro/Nanoengineering*. 2006;1(3):181-184. DOI:10.2961/jlmn.2006.03.0006

88. Lagomarsino S, Bellini M, Corsi C, Fanetti S, et al. Electrical and Raman-imaging characterization of laser-made electrodes for 3D diamond detectors. *Diamond and Related Materials*. 2014;43:23-28. DOI:10.1016/j.diamond.2014.01.002

89. Kulnitsky BA, Perezhogin IA, Blank VD. Polytypes and twins in the diamond – lonsdaleite system. *Izvestiya vysshikh uchebnykh zavedeniy. Seriya Khimiya i khimicheskaya tekhnologiya = ChemChemTech*. 2015;5(58):48-50. (In Russ.)

90. Ying P, Gao Y, Zhang B, Wu Y, et al. Synthesis of twin-structured nanodiamond particles. *AIP Advances*. 2020;10(1):015240. DOI:10.1063/1.5141035

Appendix

Different DLA calculation schemes with Moore and/or von Neumann Neighborhoods

P.1. Algorithm for fiber model construction

The algorithm for constructing the fiber model in the DLA approach was developed from the following steps (Fig. P.1): (1) At the initialization stage, a starting structure consisting of a system of seed particles located on the lower boundary was generated within the calculation area with a uniform grid, and the fiber size (maximum number of particles in the calculation area) was set; (2) A specified number of particles were generated at the upper boundary of the calculation area; (3) These particles performed random shifts downward and sideways with equal or different probabilities; (4) If they approached an occupied cell within the Moore neighborhood (Fig. P.1b), they aggregated with the occupied cell; otherwise, they continued moving; (5) Steps 2-4 were repeated.

The criterion for stopping the iterative process was the fiber reaching the required size, when the number of particles in the calculation area reached the set value, or when the nanowire reached the upper boundary of the calculation area.

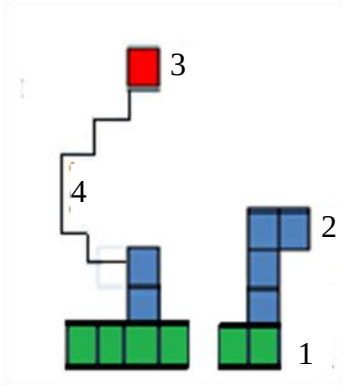

Fig. P.1a. DLA fiber model calculation scheme:
1 – starting structure, 2 – aggregated particles, 3 – new particle, 4 – random shifts. Explanations are provided in the text

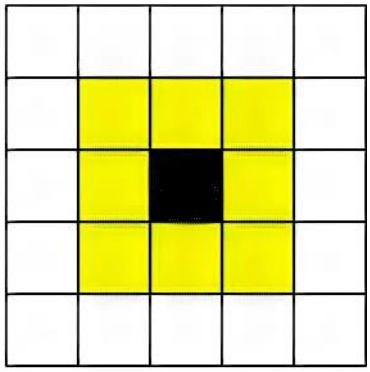

Fig. P.1b. Moore neighborhood of 8 objects

P.2. Two models of growth over inhomogeneity – random growth during particle deposition in percolation

To describe the algorithm, two functions are used: the average surface height $\overline{h(t)}$, which defines the baseline position for the surface of the sample being studied, and its roughness, $W(t)$.

In the first random growth model, all growth columns are filled randomly (Fig. P.2*a*). Then, after the random deposition of N particles, the height of the deposited structure h can be calculated using the equation:

$$h = \sqrt{Nf(1-f)+(Nf)^2},$$

where $f = 1/L$ is the probability of filling a given column, and L is the width of the calculation area, i.e., $h^i = h^{i-1} + 1$, where i is the time step [68].

In the other model of ballistic percolation deposition, a particle is fixed at the point of first contact with the already deposited structure, following the nearest neighbor rule (Fig. P.2b). In this case, the height is determined by the heights of the nearest left and right columns, and the height is calculated as the maximum of the neighboring columns' heights:

$$h_j = \max\{(h_{j-1}, h_j + 1, h_{j+1}),$$

where j is the number of the column being considered [69]. Unlike the previous model (Fig. P.2*a*), in this case, the particle can attach to the side surface of the already formed structure (Fig. P.2*a*) [70]. This means that the possibility of growth along the local normal to the surface is considered, which can lead to the expansion of local protrusions on the growth front surface, thus enhancing surface growth in the lateral direction.

The percolation structure is represented as a square grid of size m × m a. u. The cells of this grid contain either 0 (empty site) or 1 (occupied site). Each cell in the model is occupied by a particle with probability s, independent of the state of neighboring cells. For each grid cell, a random number α is generated. If $\alpha \le s$, the value in the cell is set to 1; otherwise, it is 0 (cf. with [71]). Here, the parameter s represents the percolation threshold, above which a particle is not fixed in the cell.

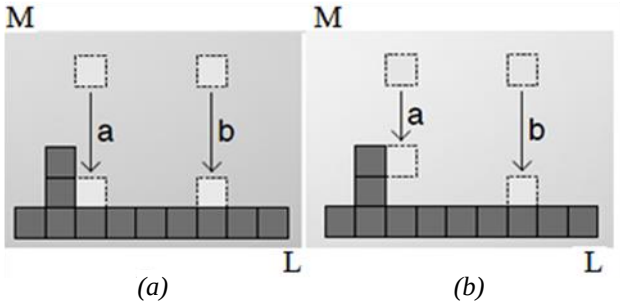

(a) *(b)*

Fig. P.2. Diagram of both (*a)* Random and *(b*) Ballistic the deposition processes for Deposited Particles – also, the moving particles labeled as letters both *a* and *b*

P.3. DLA model in the iterative algorithm

The initial state of the system was described by placing model particles, such as Au particles, along the lower boundary, serving as aggregation centers. Each iteration began by introducing a new model particle into the calculation area. The particle was introduced at a random location along the upper boundary, within its central third. This simulates the experiment where a laser beam with a diameter of 1/3 of the calculation area length is applied. Then, the standard DLA procedure was followed (Fig. P.3).

The random walk of the particle occurred from the upper boundary of the calculation area, where a notional cathode was located, to the lower boundary, where a notional anode was located. If an occupied area appeared in the Moore neighborhood of the wandering particle, it would aggregate with that area with a given probability.

To describe the random walk, a uniform grid was applied to the calculation area. Thus, the random walk was formed by a series of single-cell movements across the calculation area with a specified probability. Periodic boundary conditions were used along the sides, causing the particle to reflect off them. At the lower boundary, an adhesion condition was applied, fixing the particle in place. Varying the probabilities of individual random movements allowed for consideration of growth direction. Aggregation of the wandering particle occurred with a given probability when it encountered an occupied cell in the Moore neighborhood. In terms of physics, the aggregation probability can be understood as a conditional surface tension coefficient in the system, inversely proportional to temperature, normalized to the phase transition temperature [73].

To model experimental samples, a random nanowire model was proposed [74], where a system of random lines of equal thickness was generated on a two-dimensional calculation area. Each line was assigned a random length L from the interval [L_{min}; L_{max}]; the area had a width w. A line was defined by two points (x_1, y_1) and (x_2, y_2) with random coordinates as follows:

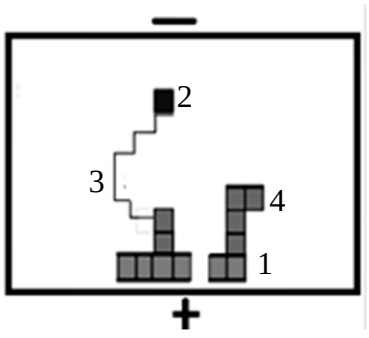

Fig. P.3. Model Diagram (One Iteration of the DLA Process): 1 – Au particles, 2 – C chain, 3 – its random walk, 4 – previously formed structure. The signs (+) and (–) correspond to the direction of the applied external electric field

$$x_c = rw; \quad y_c = rL; \quad \theta = 2\pi r;$$

$$x_2 = x_c + L\cos(\theta)/2; \quad y_2 = y_c + L\sin(\theta)/2;$$

$$x_1 = x_c - L\cos(\theta)/2; \quad y_1 = y_c - L\sin(\theta)/2,$$

where r is a random number with a uniform distribution, and θ is the angle of rotation of the wire segment.

P.4. Model for an individual microsponge

Figure P.4 presents calculations based on the proposed model: laser radiation was assumed to act on the lower boundary, where the anode (charge (+)) was located. Objects of different sizes were generated, moving with a given speed toward the upper boundary, where the cathode (charge (–)) was located.

The calculation area was conventionally divided into three subregions: two with a side length of 33 a. u., and the uppermost one with a length of 34 relative units. In these areas, the object movement speeds decreased to 3 a. u., 2 a. u., and 1 relative a. u., respectively. The probability of object merging was 20 %. The sizes of the model objects varied from 1 to 5 a. u. For example, Fig. P.4*a* shows the case of forming a sponge from small elements; Fig. P.4*b* illustrates the formation of individual elongated threads; in Fig. P.4*c*, several small sponges are generated; and in Fig. P.4*d*, most objects have merged into one large elongated sponge.

P.5. Helicoidal structure model

The diffusion model of a helicoidal structure was based on solving the diffusion equation in a discrete area using cellular automaton techniques [78]. The structure was synthesized iteratively, starting from an initial shape, where a cell in the calculation area would become occupied with a given probability if it had a neighboring occupied cell within the Moore neighborhood (considering 8 adjacent cells, as shown in Fig. P.5). The main parameter of the model was the probability of a cell being occupied. This relative model parameter can be related to a physical parameter of the system, such as the intensity of an external magnetic field in the corresponding experimental geometry.

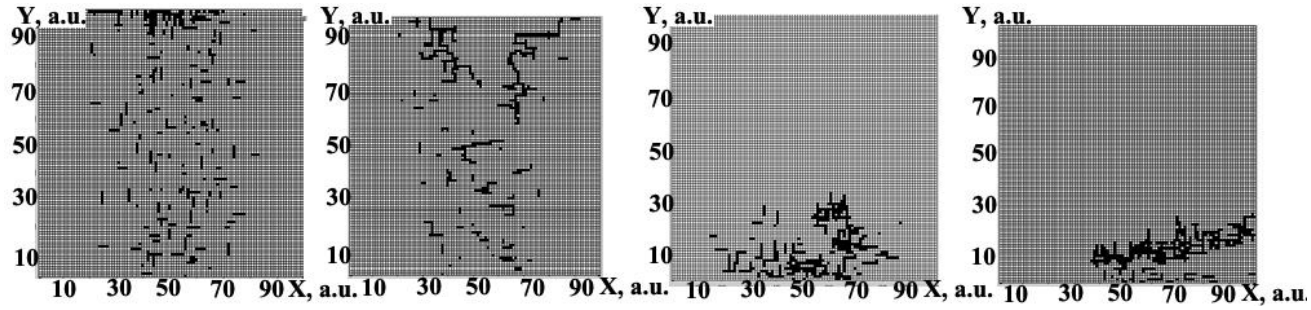

Fig. P.4. Model of a sponge system made from individual threads (in the horizontal plane relative to the boundary): a system of small sponges made of short threads, located near the upper boundary of the calculation area (*a*); a system of vertically elongated sponges, made of individual long threads, localized near the upper boundary of the calculation area (*b*); a system of small sponges with a relatively uniform structure, localized near the lower boundary of the calculation area (*c*); a system of sponges made from one large elongated object, located near the lower boundary of the calculation area (*d*)

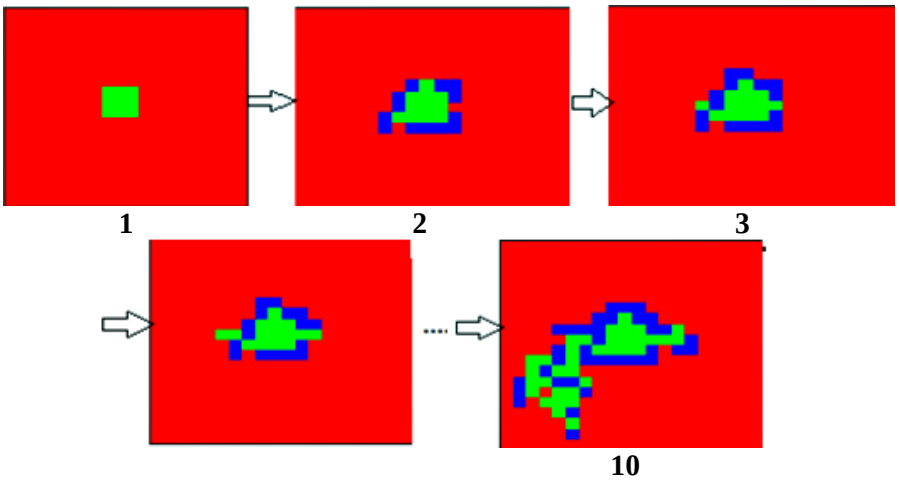

Fig. P.5. Model diagram: the resulting helical structure after performing 1–10 iterations, starting from the initial shape numbered 1 (explanations are provided in the text).

Information about the authors / Информация об авторах

Dmitry N. Bukharov, Cand. Sc. (Phys. and Math.), Associate Professor, Vladimir State University (VlSU), Vladimir, Russian Federation; ORCID 0000-0002-4536-8576; e-mail: buharovdn@gmail.com

Darya D. Tumarkina, Teaching Assistant; VlSU, Vladimir, Russian Federation; ORCID 0009-0007-5496-4234; e-mail: tumarkina.darya@mail.ru

Alexey O. Kucherik, D. Sc. (Phys. and Math.), Associate Professor, Vice-Rector for Research and Digital Development, VlSU, Vladimir, Russian Federation; ORCID 0000-0003-0589-9265; e-mail: kucherik@vlsu.ru

Alexey G. Tkachev, D. Sc. (Eng.), Professor, Head of the Department, Tambov State Technical University (TSTU), Tambov, Russian Federation; ORCID 0000-0001-5099-9682; e-mail: nanotam@yandex.ru

Sergei M. Arakelian, D. Sc. (Phys. and Math.), Professor, Independent Researcher, Vladimir, Russian Federation; ORCID 0000-0002-6323-7123; e-mail: arak@vlsu.ru

Irina V. Burakova, Cand. Sc. (Eng.), Associate Professor, TSTU, Tambov, Russian Federation; ORCID 0000-0003-0850-9365; e-mail: iris_tamb68@mail.ru

Alexander E. Burakov, Cand. Sc. (Eng.), Associate Professor, TSTU, Tambov, Russian Federation; ORCID 0000-0003-4871-3504; e-mail: m-alex1983@yandex.ru

Бухаров Дмитрий Николаевич, кандидат физико-математических наук, доцент, Владимирский государственный университет имени А. Г. и Н. Г. Столетовых (ВлГУ), Владимир, Российская Федерация; ORCID 0000-0002-4536-8576; e-mail: buharovdn@gmail.com

Тумаркина Дарья Денисовна, ассистент преподавателя, ВлГУ, Владимир, Российская Федерация; ORCID 0009-0007-5496-4234; e-mail: tumarkina.darya@mail.ru

Кучерик Алексей Олегович, доктор физико-математических наук, доцент, проректор по научной работе и цифровому развитию, ВлГУ, Владимир, Российская Федерация; ORCID 0000-0003-0589-9265; e-mail: kucherik@vlsu.ru

Ткачев Алексей Григорьевич, доктор технических наук, профессор, заведующий кафедрой, Тамбовский государственный технический университет (ТГТУ), Тамбов, Российская Федерация; ORCID 0000-0001-5099-9682; e-mail: nanotam@yandex.ru

Аракелян Сергей Мартиросович, доктор физико-математических наук, профессор, независимый исследователь, Владимир, Российская Федерация; ORCID 0000-0002-6323-7123; e-mail: arak@vlsu.ru

Буракова Ирина Владимировна, кандидат технических наук, доцент, ТГТУ, Тамбов, Российская Федерация; ORCID 0000-0003-0850-9365; e-mail: iris_tamb68@mail.ru

Бураков Александр Евгеньевич, кандидат технических наук, доцент, ТГТУ, Тамбов, Российская Федерация; ORCID 0000-0003-4871-3504; e-mail: m-alex1983@yandex.ru

Received 30 April 2024; Accepted 28 June 2024; Published 22 October 2024